

WL-TR-93-3065

AIRCRAFT WHEEL LIFE ASSESSMENT

AD-A274 378



B.F. SPENCER JR., D.J. KIRKNER,
E.E. SCHUDT, AND S. KANDARPA

UNIVERSITY OF NOTRE DAME
DEPARTMENT OF CIVIL ENGINEERING
& GEOLOGICAL SCIENCES
NOTRE DAME IN 46556-0767

JULY 1993

FINAL REPORT FOR 10/01/91-09/01/92

APPROVED FOR PUBLIC RELEASE; DISTRIBUTION IS UNLIMITED.

S DTIC
ELECTE
DEC 28 1993
A

FLIGHT DYNAMICS DIRECTORATE
WRIGHT LABORATORY
AIR FORCE MATERIEL COMMAND
WRIGHT PATTERSON AFB OH 45433-7562

93 12 23 003

1288

93-31146

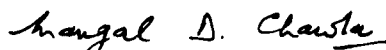


NOTICE

When Government drawings, specifications, or other data are used for any purpose other than in connection with a definitely Government-related procurement, the United States Government incurs no responsibility or any obligation whatsoever. The fact that the government may have formulated or in any way supplied the said drawings, specifications, or other data, is not to be regarded by implication, or otherwise in any manner construed, as licensing the holder, or any other person or corporation; or as conveying any rights or permission to manufacture, use, or sell any patented invention that may in any way be related thereto.

This report is releasable to the National Technical Information Service (NTIS). At NTIS, it will be available to the general public, including foreign nations.

This technical report has been reviewed and is approved for publication.



MANGAL D. CHAWLA, Proj Engr
Landing Gear Systems Section
Aircraft Launch & Recovery Branch



AIVARS V. PETERSONS, Chief
Aircraft Launch & Recovery Branch
Vehicle Subsystems Division



RICHARD E. COLCLOUGH JR.
Chief
Vehicle Subsystems Division

IF YOUR ADDRESS HAS CHANGED, IF YOU WISH TO BE REMOVED FROM OUR MAILING LIST, OR IF THE ADDRESSEE IS NO LONGER EMPLOYED BY YOUR ORGANIZATION PLEASE NOTIFY WL/FIVMA, WRIGHT-PATTERSON AFB, OH 45433-7202 TO HELP MAINTAIN A CURRENT MAILING LIST.

COPIES OF THIS REPORT SHOULD NOT BE RETURNED UNLESS RETURN IS REQUIRED BY SECURITY CONSIDERATIONS, CONTRACTUAL OBLIGATIONS, OR NOTICE ON A SPECIFIC DOCUMENT.

REPORT DOCUMENTATION PAGE

Form Approved
OMB No. 0704-0188

Public reporting burden for this collection of information is estimated to average 1 hour per response, including the time for reviewing instructions, searching existing data sources, gathering and maintaining the data needed, and completing and reviewing the collection of information. Send comments regarding this burden estimate or any other aspect of this collection of information, including suggestions for reducing this burden, to Washington Headquarters Services, Directorate for Information Operations and Reports, 1215 Jefferson Davis Highway, Suite 1204, Arlington, VA 22202-4302, and to the Office of Management and Budget, Paperwork Reduction Project (0704-0188), Washington, DC 20503.

1. AGENCY USE ONLY (Leave blank)		2. REPORT DATE JUL 1993	3. REPORT TYPE AND DATES COVERED FINAL 10/01/91 - 09/01/92	
4. TITLE AND SUBTITLE AIRCRAFT WHEEL LIFE ASSESSMENT			5. FUNDING NUMBERS C FE 63205 FR 2978 TA 01 WU 06	
6. AUTHOR(S) B. F. SPENCER, JR., D. J. KIRKNER, E. E. SCHUDT, AND S. KANDARPA				
7. PERFORMING ORGANIZATION NAME(S) AND ADDRESS(ES) UNIVERSITY OF NOTRE DAME DEPARTMENT OF CIVIL ENGINEERING & GEOLOGICAL SCIENCES NOTRE DAME IN 46556-0767			8. PERFORMING ORGANIZATION REPORT NUMBER	
9. SPONSORING / MONITORING AGENCY NAME(S) AND ADDRESS(ES) FLIGHT DYNAMICS DIRECTORATE WRIGHT LABORATORY AIR FORCE MATERIEL COMMAND WRIGHT PATTERSON AFB OH 45433-7562			10. SPONSORING / MONITORING AGENCY REPORT NUMBER WL-TR-93-3065	
11. SUPPLEMENTARY NOTES				
12a. DISTRIBUTION / AVAILABILITY STATEMENT APPROVED FOR PUBLIC RELEASE; DISTRIBUTION IS UNLIMITED.			12b. DISTRIBUTION CODE	
13. ABSTRACT (Maximum 200 words) The important part of wheel life assessment problems is the accurate determination of the tire/wheel interface pressure distribution under various loading conditions. A combined analytical/experimental methodology for obtaining this pressure distribution was developed. The principal analytical tool in this methodology is the finite element program ANTWIL (Analysis of Tire Wheel Interface Loads) which recovers the pressure distribution given a number of experimental strain measurements on the wheel. The major activity consisted of a study of the F-16 Block 30 and the Block 40 main landing gear wheels to determine the optimal number and location of the strain gages for subsequent experiments. Experiments to be conducted will record strains at the specified locations and this data will be used to determine tire/wheel interface pressures.				
14. SUBJECT TERMS TIRE/WHEEL INTERFACE, PRESSURE DISTRIBUTION, EXPERIMENTAL STRAINS, FINITE ELEMENT PROGRAM			15. NUMBER OF PAGES 61	
			16. PRICE CODE	
17. SECURITY CLASSIFICATION OF REPORT UNCLASSIFIED	18. SECURITY CLASSIFICATION OF THIS PAGE UNCLASSIFIED	19. SECURITY CLASSIFICATION OF ABSTRACT UNCLASSIFIED	20. LIMITATION OF ABSTRACT UL	

Table of Contents

1.0	Introduction.....	1
2.0	Tire-Wheel Interface Load Recovery	3
2.1	Introduction.....	3
2.2	Theoretical Development of Load Recovery Algorithm	3
2.3	Numerical Experiments	9
	2.3.1 Block 30 Wheel	10
	2.3.2 Block 30 Wheel: Optimal Locations	17
	2.3.3 Block 40 Wheel	17
2.4	Shear Traction	20
	2.4.1 Numerical Experiments.....	25
3.0	Crack Initiation: Literature Review	27
3.1	Introduction.....	27
3.2	Models Based on Slip Band Theory	27
3.3	Continuum Damage Mechanics Models.....	28
	3.3.1 Stochastic Models.....	29
	3.3.2 Summary.....	30
4.0	Residual Stresses: Literature Review.....	31
4.1	Introduction.....	31
4.2	Residual Stresses: Literature Review.....	31
5.0	Summary of Work Performed in FY 92.....	33
6.0	Planned Tasks: FY 93	34
7.0	Closure	38
8.0	References.....	39
	Appendix A- Finite Element Formulation.....	43
	Appendix B- Surface Traction and Load Distributions.....	49

DTIC QUALITY INSPECTED 8

Accession For	
NTIS CRA&I	<input checked="" type="checkbox"/>
DTIC TAB	<input type="checkbox"/>
Unannounced	<input type="checkbox"/>
Justification	
By	
Distribution /	
Availability Codes	
Dist	Avail and/or Special
A-1	

List of Figures

Figure		Page
1	Cross-Section of F-16 Block 30 Wheel (showing sectioned area only)	4
2	A figure showing the r , z and s coordinates, and interface pressure	5
3	(a) Axisymmetric Body (b) Direction of Vector g at which Strains are Computed	7
4	Hypothetical Load on Bead Seat Region	9
5	Comparison of Analytical and Recovered Load. (--- recovered load, — applied load; Rosettes: 4 out, 4 in, 2 flange).....	10
6	Comparison of Analytical and Recovered Load. (--- recovered load, — applied load; Rosettes: 4 out, 3 in, 2 flange).....	11
7	Comparison of Analytical and Recovered Load. (--- recovered load, — applied load; Rosettes: 4 out, 2 in, 2 flange).....	12
8	Comparison of Analytical and Recovered Load. (--- recovered load, — applied load; Rosettes: 4 out, 3 in, 3 flange).....	13
9	Comparison of Analytical and Recovered Load. (--- recovered load, — applied load; Rosettes: 4 out, 2 in, 3 flange).....	13
10	Comparison of Analytical and Recovered Load Varying Location on Flange. (--- recovered load, — applied load; Rosettes: 4 out, 3 in, 2 flange).....	14
11	Results of ANTWIL for First Mode for Loads Applied and Recovered in the $s(r,z)$ Direction. (--- recovered load, — applied load; Rosettes: 4 out, 3 in, 2 flange).....	15
12	Results of ANTWIL for Second Mode for Loads Applied and Recovered in the $s(r,z)$ Direction. (--- recovered load, — applied load; Rosettes: 4 out, 3 in, 2 flange).....	15
13	Results of ANTWIL for Third Mode for Loads Applied and Recovered in the $s(r,z)$ Direction. (--- recovered load, — applied load; Rosettes: 4 out, 3 in, 2 flange).....	16
14	Results of ANTWIL for the Mirror Image Load. (--- recovered load, — applied load; Rosettes: 4 out, 3 in, 2 flange).....	16
15	Locations of Strain Gages for F-16 Block 30 Wheel.....	18
16	Locations of the Optimal Number of Strain Gages for the F-16 Block 40 Wheel.	20
17	Results of ANTWIL for Nine Gage Configuration (--- recovered load, — applied load; Rosettes: 4 out, 3 in, 2 flange).....	21
18	Results of ANTWIL for Zeroth Harmonic for Loads Applied and Recovered in the $s(r,z)$ Direction: Eight Gage Configuration (--- recovered load, — applied load; Rosettes: 4 out, 4 in.)	21
19	Results of ANTWIL for First Harmonic for Loads Applied and Recovered in the $s(r,z)$ Direction: Eight Gage Configuration (--- recovered load, — applied load; Rosettes: 4 out, 4 in.)	22
20	Results of ANTWIL for Second Harmonic for Loads Applied and Recovered in the $s(r,z)$ Direction: Eight Gage Configuration (--- recovered load, — applied load; Rosettes: 4 out, 4 in.)	22

21	Results of ANTWIL for Third Harmonic for Loads Applied and Recovered in the $s(r,z)$ Direction: Eight Gage Configuration (--- recovered load, — applied load; Rosettes: 4 out, 4 in.)	23
22	Results of ANTWIL for Zeroth Harmonic Using a Mirror Image Load: Eight Gage Configuration (--- recovered load, — applied load; Rosettes: 4 out, 4 in.)	23
23	Results of ANTWIL for First Harmonic Using a Mirror Image Load: Eight Gage Configuration (--- recovered load, — applied load; Rosettes: 4 out, 4 in.)	24
24	Results of ANTWIL for the Second Harmonic Using a Mirror Image Load: Eight Gage Configuration (--- recovered load, — applied load; Rosettes: 4 out, 4 in.)	24
25	Results of ANTWIL for Third Harmonic Using a Mirror Image Load: Eight Gage Configuration (--- recovered load, — applied load; Rosettes: 4 out, 4 in.)	25
26	Results of ANTWIL: Recovery of Shear Traction (--- recovered load, — applied load; Rosettes: 4 out, 3 in, 2 flange)	26
27	Model of F-16 Block 30 Main Landing Gear Wheel	34
A-1	Axisymmetric Body with Triangular Elements.	43
A-2	(a) Symmetric Loads with Respect to $\theta = 0$ Due to Cosine Terms. (b) Asymmetric Loads with Respect to $\theta = 0$ Due to Sine Terms.	46
B-1	Eight-Noded Isoparametric Element with a Load of $q(s)$	49
B-2	Load pds Acting Over an Differential Element ds	51
B-3	Eight-Noded Element. $A, B, C,$ and D are Barlow Points.	53
B-4	(a) Axisymmetric Body (b) Direction of g at Which Strains are Computed.	54
B-5	Side of an Eight-Noded Isoparametric Element Where $\eta = 1$. Point P is Where Strains are Computed.	55

1.0 Introduction

This is the report for fiscal year 1992 on the project "Aircraft Wheel Life Assessment" funded by the Landing Gear Systems Section of the Flight Dynamics Directorate at Wright-Patterson Air Force Base.

It has been determined that an important part of the wheel life assessment problem is the accurate determination of the tire-wheel interface pressure distribution under various loading conditions. A combined analytical/experimental methodology for obtaining this pressure distribution was developed at the University of Notre Dame. The principle analytical tool in this methodology is the finite element program ANTWIL (ANalysis of Tire-Wheel Interface Loads) [Kandarpa *et al.*, 1991) which recovers the pressure distribution given a number of experimental strain measurements on the wheel. The major activity on this project in FY92 consisted of a study of the F-16 Block 30 and the Block 40 main landing gear wheels to determine the optimal number and location of the strain gages for subsequent experiments. Experiments to be conducted at WPAFB will record strains at the locations specified, and these data will be used to determine the tire-wheel interface pressure distributions for each test case. Modifications have been made to ANTWIL to expand its capability. The ability to recover a circumferential shear traction has been incorporated into the code. Ongoing work and planned tasks for FY93 are delineated.

Landing gear wheel failures have been responsible for a significant amount of aircraft damage. Many such wheel failures have been catastrophic, resulting in a sudden loss of tire inflation pressure and, consequently, severe damage to primary aircraft structures. An FAA study, by Dupur and Brussat [1985], showed that more than 30 percent of the over 5,000 operational failures reported from 1970-1975 were due to wheel problems. This does not include wheels which were removed from service ahead of their expected service life because of cracks found during routine tire changes.

The Landing Gear Systems Section, WL/FIVMA, at Wright-Patterson Air Force Base initiated an inhouse program in late 1986 to investigate experimental and analytical methods for wheel life estimation and verification [Treanor and Carter, 1987; Treanor and Boike, 1988]. As part of this effort, preliminary studies were conducted at the University of Notre Dame to determine the propagation behavior of cracks in the bead seat region [Enneking, 1987; Lawler, *et al.*, 1989]. While the results of the effort were successful, the research identified a need to determine the load distribution at the tire-wheel interface and the distribution of time to crack initiation in order to accurately predict the crack propagation life of a wheel in the bead seat region. Subsequent wheels mounted with radial tires have failed due to cracks forming in other parts of the wheel (*e.g.*, near the lightning holes). Therefore, accurate knowledge of the stresses at arbitrary locations in the wheel is necessary. The tire-wheel interface loads are also necessary for such stress determination.

The University of Notre Dame has completed development and implementation of an experimental/analytical methodology which will allow for determination of the loads at the tire-wheel interface. A finite element code, ANTWIL, has been developed which will run on a computer workstation in the WL/FIVMA laboratory and can directly yield the tire-wheel interface pressure distribution given appropriate strain gage measurements [Kandarpa *et al.*, 1991]. The ANTWIL program employs an axisymmetric finite element model which is subjected to asymmetric loading. The loading is represented as a double Fourier series, and the components are determined by a least squares fit using the experimentally determined strains.

Below we review the work completed during this fiscal year. Following this, the tasks are discussed that have been identified for the 1993 fiscal year to support efforts in determining aircraft wheel life.

2.0 Tire-Wheel Interface Load Recovery

2.1 Introduction

One of the research efforts in FY 92 involved finding the optimal number and location of strain gages necessary to capture the essential features of the tire-wheel interface pressure distribution. These locations were subsequently given to WL/FIVMA laboratory for testing. The information obtained from these experiments will be used as input data for ANTWIL, and the tire-wheel interface pressure will be back-calculated to verify the proposed methodology. In the next few paragraphs, we will discuss the analytical experiments that were performed for determining the optimal number and location of strain gages. First, the load recovery algorithm is reviewed for completeness.

2.2 Theoretical Development of Load Recovery Algorithm

Consider the aircraft wheel depicted in Fig. 1. The geometry of the wheel and strain measurements at discrete points on the wheel surface are assumed to be available. From knowledge of the geometry and the boundary conditions of the wheel, an axially symmetric finite element model is developed which is subjected to asymmetric loading (see Appendix A). This model will be used to *back-calculate* the load distribution at the tire-wheel interface (also known as the bead seat region) from the strain measurements.

Although the geometry of the wheel, in general, is not axially symmetric due to lightening holes, brake lugs, etc., the wheel can be reasonably approximated as an axially symmetric body because the input analysis data is obtained in regions removed from geometric irregularities. By using this geometric simplification, analysis can be carried out on a two-dimensional axisymmetric domain (r, z) rather than the original three-dimensional body, thus, greatly reducing the computational effort.

In the proposed problem where tire-wheel interface loads are to be computed, the loading is not only asymmetric but also varies along the surface (s) of the body. Herein, we use a cylindrical coordinate system r, θ, z (see Fig. 2). The surface load is expressed as a function of θ and s where s , the surface coordinate, is a function of r and z . The loading can be represented as a Fourier series in θ and s . In the algorithm development that follows, the tractions are assumed to be normal to the wheel surface. However, in the theory presented, the load $p(\theta, s)$ can represent any loading component, including surface tractions. The load $p(\theta, s)$ is, thus, given by:

$$p(\theta, s) = \sum_n [p_{cn}(s) \cos(n\theta) + p_{sn}(s) \sin(n\theta)]$$

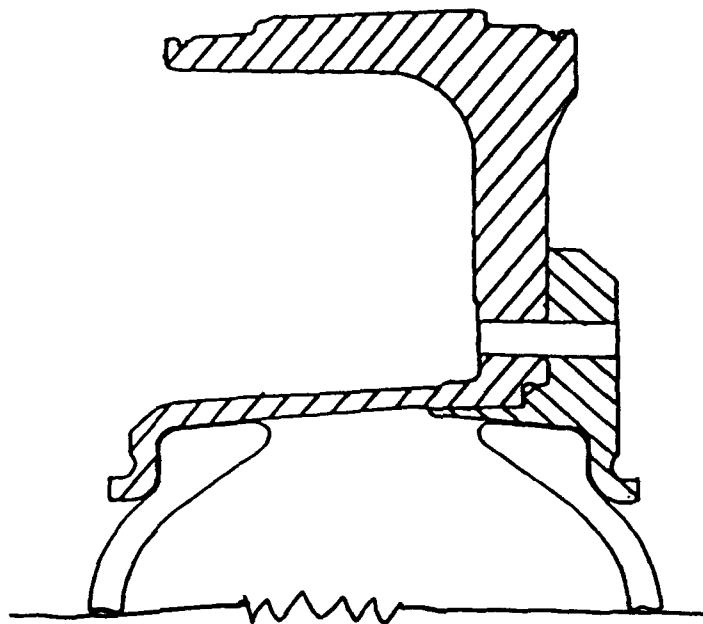
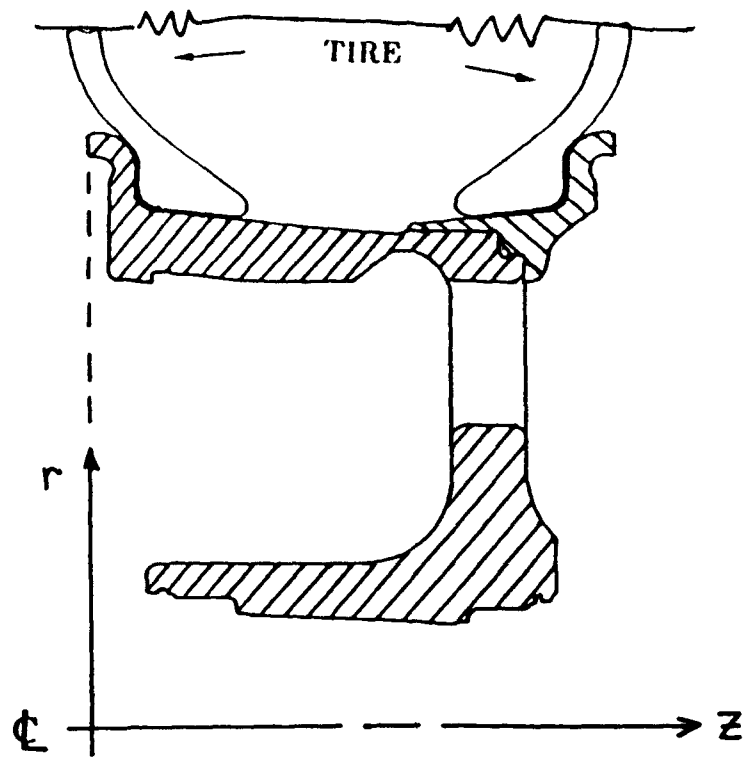


FIGURE 1: Cross-Section of F-16 Block 30 Wheel (showing sectioned area only).

Further, we may expand the coefficients $p_{cn}(s)$, $p_{sn}(s)$ in Fourier series over the interval of loading defined to be $0 < s < L$. Without loss of generality we use a Fourier cosine series. The final series representation is then given by:

$$p(\theta, s) = \sum_m \sum_n \{ p_{cnm} \cos(n\theta) \cos(m \frac{\pi s}{L}) + p_{snm} \sin(n\theta) \cos(m \frac{\pi s}{L}) \}. \quad (1)$$

Consider a single loading component of unit amplitude:

$$\cos(n\theta) \cos(m \frac{\pi s}{L}). \quad (2)$$

Let the strain response due to the above load be $\epsilon_{cnm}(r, \theta, z)$. All strains calculated in this paper are based on a linear elastic and isotropic material response. The strain tensor at a point due to this loading can be decomposed as follows:

$$\epsilon_{cnm}(r, \theta, z) = \epsilon_{cnm}^c(r, z) \cos(n\theta) + \epsilon_{cnm}^s(r, z) \sin(n\theta), \quad (3)$$

where ϵ_{cnm}^c and ϵ_{cnm}^s are the cosine and sine amplitudes. If the load amplitude were p_{cnm} rather than unity, then the strain response would be $p_{cnm} \epsilon_{cnm}$. Similarly, the response due to a *sine* component loading:

$$\sin(n\theta) \cos(m \frac{\pi s}{L}) \quad (4)$$

in the θ -direction would be written as:

$$\epsilon_{snm}(r, \theta, z) = \epsilon_{snm}^c(r, z) \cos(n\theta) + \epsilon_{snm}^s(r, z) \sin(n\theta). \quad (5)$$

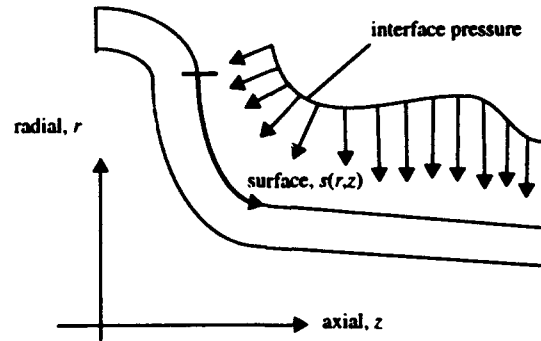


FIGURE 2. A figure showing the r, z and s coordinates, and interface pressure.

The tensor coefficients, ϵ_{cnm}^c and ϵ_{snm}^s , in equations (2) and (3) have the structure,

$$\epsilon^c = \begin{bmatrix} \epsilon_r^c & 0 & \gamma_{rz}^c/2 \\ 0 & \epsilon_\theta^c & 0 \\ \gamma_{rz}^c/2 & 0 & \epsilon_z^c \end{bmatrix}, \quad (6)$$

whereas ϵ_{cnm}^s and ϵ_{snm}^s have the structure,

$$\epsilon^s = \frac{1}{2} \begin{bmatrix} 0 & \gamma_{r\theta}^s & 0 \\ \gamma_{r\theta}^s & 0 & \gamma_{\theta z}^s \\ 0 & \gamma_{\theta z}^s & 0 \end{bmatrix}. \quad (7)$$

The total response due to the loading as given in equation (1), by superposition, would then be:

$$\begin{aligned} \epsilon(r, \theta, z) &= \sum_n \sum_m \{ p_{cnm} \epsilon_{cnm}^c + p_{snm} \epsilon_{snm}^s \} \\ &= \sum_n \sum_m \{ p_{cnm} [\epsilon_{cnm}^c \cos(n\theta) + \epsilon_{cnm}^s \sin(n\theta)] \\ &\quad + p_{snm} [\epsilon_{snm}^c \cos(n\theta) + \epsilon_{snm}^s \sin(n\theta)] \} \end{aligned}$$

Since strain measurements will be taken on the surface of the body, an expression is needed for the direct strain on the surface in a specified direction. Referring to Fig. 3, it is required to find the strain on the surface of the body of revolution at a point with surface coordinate s and in a direction characterized by the unit vector \mathbf{g} , defined with reference to Fig. 3 by (see Appendix B):

$$\mathbf{g} = -\mu \sin(\varphi) \mathbf{e}_r + \cos(\varphi) \mathbf{e}_\theta + \lambda \sin(\varphi) \mathbf{e}_z \quad (8)$$

where μ and λ are direction cosines of the unit tangential vector \mathbf{e}_t and φ is the angle between the strain gage placed on the surface of the body and the circumferential direction \mathbf{e}_θ .

If $\epsilon(\theta, s)$ is the strain tensor of equation (8) evaluated at the point of interest on the surface then the required direct strain is given by:

$$\epsilon_g(\theta, s) = \mathbf{g}^T \epsilon(\theta, s) \mathbf{g} \quad (9)$$

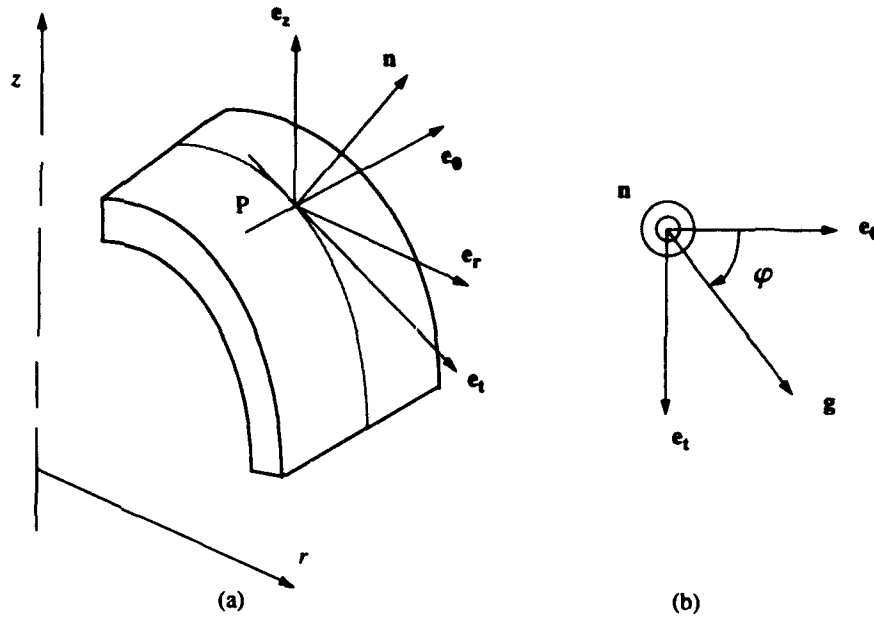


FIGURE 3. (a) Axisymmetric Body (b) Direction of Vector g at which Strains are Computed.

Thus, we can write the series expansion for this direct strain as:

$$\begin{aligned} \epsilon(\theta, s) = & \sum_n \sum_m p_{cnm} [\epsilon_{cnm}^c \cos(n\theta) + \epsilon_{cnm}^s \sin(n\theta)] + \\ & p_{snm} [\epsilon_{snm}^c \cos(n\theta) + \epsilon_{snm}^s \sin(n\theta)] \end{aligned} \quad (10)$$

where the subscript g is dropped for simplicity, but it should be kept in mind that all the strains in equation (10) are obtained by application of equation (9) to the component strain tensors of equations (6) and (7). Also, note that equation (10) may be reordered as:

$$\begin{aligned} \epsilon(\theta, s) = & \sum_n \sum_m (p_{cnm} \epsilon_{cnm}^c + p_{snm} \epsilon_{snm}^c) \cos(n\theta) \\ & (p_{cnm} \epsilon_{cnm}^s + p_{snm} \epsilon_{snm}^s) \sin(n\theta) \end{aligned} \quad (11)$$

The direct strains are obtained experimentally at J locations and are denoted $\epsilon^*(s_j)$; $j = 1, \dots, J$ (in the direction defined by g as above). They may be decomposed into Fourier cosine and sine components and written as:

$$\epsilon^*(s_j) = \sum_n \{ \epsilon_{cn}^*(s_j) \cos(n\theta) + \epsilon_{sn}^*(s_j) \sin(n\theta) \} \quad (12)$$

Now comparing the cosine and sine terms of equations (11) and (12) yields,

$$\sum_{m=0}^M \{p_{cnm} \epsilon_{cnm}^c(s_j) + p_{snm} \epsilon_{snm}^s(s_j)\} = \epsilon_{cn}^*(s_j) \quad (13)$$

and:

$$\sum_{m=0}^M \{p_{cnm} \epsilon_{cnm}^s(s_j) + p_{snm} \epsilon_{snm}^c(s_j)\} = \epsilon_{sn}^*(s_j) \quad (14)$$

where the series has been truncated after M terms.

The above equations can be concisely written in matrix notation as:

$$\mathbf{E}_{nj} \mathbf{p}_n = \boldsymbol{\epsilon}_{nj}^* \quad (15)$$

where:

$$\mathbf{E}_{nj} = \begin{bmatrix} \epsilon_{cn1}^c(s_j) & \epsilon_{sn1}^c(s_j) & \dots & \epsilon_{cnM}^c(s_j) & \epsilon_{snM}^c(s_j) \\ \epsilon_{cn1}^s(s_j) & \epsilon_{sn1}^s(s_j) & \dots & \epsilon_{cnM}^s(s_j) & \epsilon_{snM}^s(s_j) \end{bmatrix} \quad (16)$$

$$\mathbf{p}_n = [p_{cn1} \ p_{sn1} \ \dots \ p_{cnM} \ p_{snM}]^T \quad (17)$$

$$\boldsymbol{\epsilon}_{nj}^* = \begin{bmatrix} \epsilon_{cn}^*(s_j) \\ \epsilon_{sn}^*(s_j) \end{bmatrix} \quad (18)$$

These equations are assembled together for all J experimental points resulting in:

$$\mathbf{E}_n \mathbf{p}_n = \boldsymbol{\epsilon}_n^* \quad (19)$$

where:

$$\mathbf{E}_n = [\mathbf{E}_{n1} \ \dots \ \mathbf{E}_{nJ}]^T$$

$$\boldsymbol{\epsilon}_n^* = [\boldsymbol{\epsilon}_{n1}^* \ \dots \ \boldsymbol{\epsilon}_{nJ}^*]^T \quad (20)$$

Finally, premultiplying equation (19) by \mathbf{E}_n^T results in the least squares equation,

$$(\mathbf{E}_n^T \mathbf{E}_n) \mathbf{p}_n = \mathbf{E}_n^T \boldsymbol{\epsilon}_n^* \quad (21)$$

Solution of equation (21) yields the amplitudes of the Fourier components, p_n . This process is repeated for all $n = 0, \dots, N$ in the θ -direction. The amplitudes p_n are substituted into equation (1) and the load distribution on the contact surface is produced.

2.3 Numerical Experiments

Sample numerical experiments were conducted in a three step sequence. First, a known analytical load (see Fig. 4) is applied on the surface of the wheel (around the bead seat region). By performing a finite element analysis, strain readings are obtained at J locations on the surface. Usually the strains were computed at the same locations as the experimental strains gages and for this reason are called the experimental strains. These strains are decomposed in their sine and cosine components and stored in a vector of length $2J$, e_n^* , where n corresponds to the harmonic number in the circumferential direction. Note that in an actual analysis, the first step is done experimentally. Next, the same analytical model is subjected to M unit harmonic loads in the s -direction, for a specific n , and strains are determined at the same locations as the experimental strains. These *analytical* strains are then stored in a matrix E_n of dimension $2J \times M$ where each column of length $2J$ corresponds to the strains due to the m^{th} Fourier load. Finally, the Fourier amplitudes p_n are obtained by solution of the least squares equation (20). These amplitudes are used for calculating the interface pressure which is then compared with the applied load for convergence and accuracy. Further details of the above procedure can be found in Kandarpa *et al.* (1991).

Using the above procedure, sample numerical experiments were conducted by using different numbers of strain gages. These results were further compared among themselves and the best configuration was chosen. Details of the analytical experiments are summarized below.

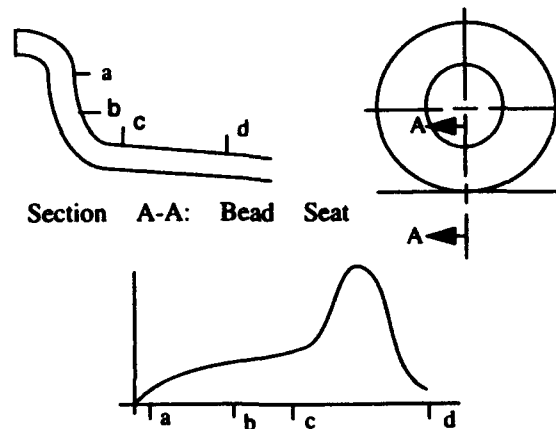


FIGURE 4. Hypothetical Load on Bead Seat Region

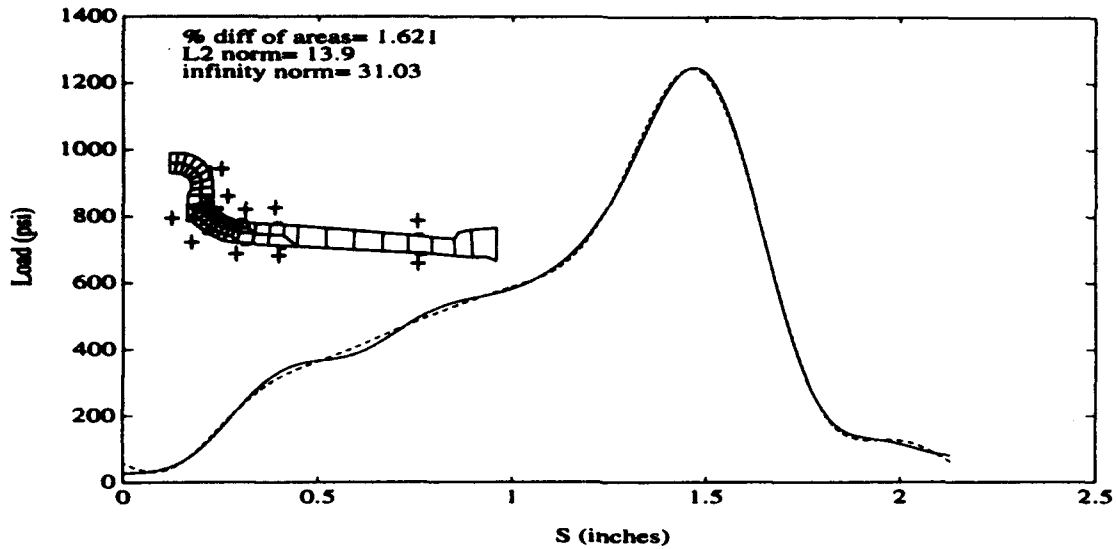


FIGURE 5. Comparison of Analytical and Recovered Load. (--- recovered load, — applied load; Rosettes: 4 out, 4 in, 2 flange)

2.3.1 Block 30 Wheel

From research performed earlier, it was determined that the best results were achieved when there was a significant number of strain gages in the loading area. It was found that eight strain gage rosettes (total, inboard and outboard sides of the wheel) in the loading area provided adequate results. Two additional rosettes were placed at the base of the flange to obtain a better recovery of the load. The need for the gages on the base of the flange was also determined from previous experiments.

The number of strain gage rosettes in the bead seat region were evenly placed along the flange on both the inside and outside surfaces. Four rosettes were placed on the inside surface and four were placed on the outside, along with the two gages on the base of the flange, for a total of 10 gages. Figure 5 shows the analytically applied load as a dashed line and the recovered load as a solid line. This configuration was used as a base of comparison as the interior rosettes were removed one at a time.

Three measures of error are given on each graph. The L_∞ -norm (denoted the infinity norm) is the absolute value of the maximum difference between the applied load $p_n(s)$ and the recovered load p_n^* , i.e.,

$$L_\infty\text{-norm} = \max_s | p_n(s) - p_n^*(s) | . \quad (22)$$

The L_2 -norm is the square root of the square of the differences integrated over the loading region, i.e.,

$$L_2\text{-norm} = \left\{ \int |p_n(s) - p_n^*(s)|^2 ds \right\}^{1/2}. \quad (23)$$

The third error measure, closely related to the L_1 - norm, is called here the *percent diff of areas*, and is defined as:

$$\% \text{ diff of areas} = \frac{\int |p_n(s) - p_n^*(s)| ds}{\int p_n(s) ds} \times 100. \quad (24)$$

The results depicted in Fig. 6 were obtained from the equal spacing of three rosettes on the inside curve for a total of nine rosettes. All error measures show this configuration to be marginally better than the previous configuration.

The number of equally spaced rosettes on the inside of the load area was then reduced to two. Again, the desired result was to decrease the number of gages on the inside surface without losing accuracy. The results are displayed in Fig. 7. The errors are close to those of the original configuration except for the L_2 -norm which is higher.

As shown in the previous figures, the optimal configuration in the loading area includes four rosettes on the outside of the load area and three rosettes on the inside of the load area. The next step was to determine the variations in the results that could be caused by adding a rosette to the area at the base of the flange. The configuration also included four rosettes on the outside of the

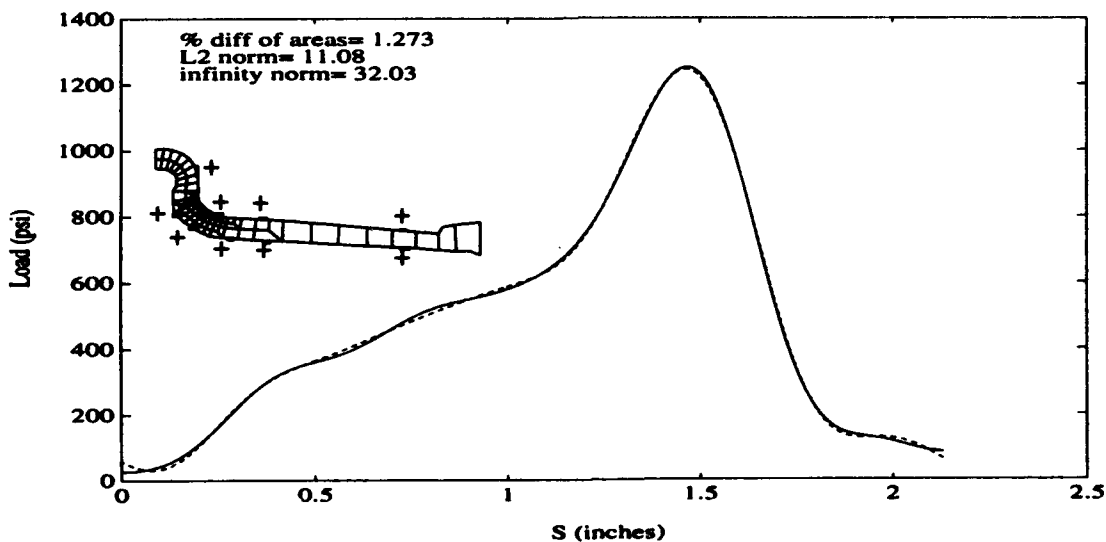


FIGURE 6. Comparison of Analytical and Recovered Load. (--- recovered load, — applied load; Rosettes: 4 out, 3 in, 2 flange)

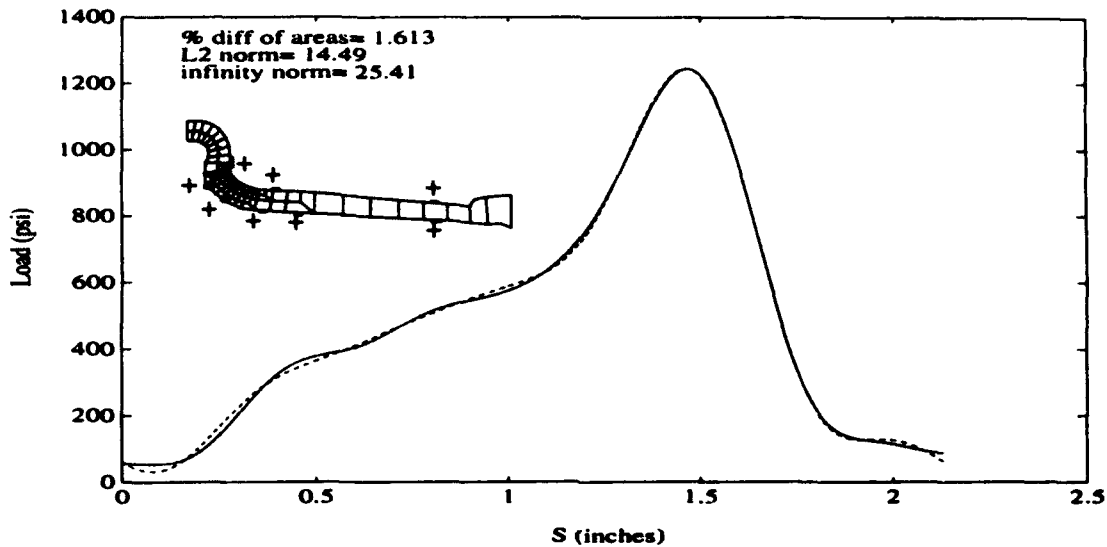


FIGURE 7. Comparison of Analytical and Recovered Load. (--- recovered load, — applied load; Rosettes: 4 out, 2 in, 2 flange)

load area, three on the inside of the load area, and the two rosettes at the base of the flange. Figure 8 illustrates the results for this configuration.

Comparing these results with the results from the configuration without the extra rosette on the base of the flange, it can be seen that the extra rosette provides redundant information. The resulting recovered load has a slightly higher error for two of the three error norms with the extra rosette on the base of the flange.

The next run was to determine if adding a rosette on the base of the flange would improve the results from the configuration with only two rosettes on the inside and four on the outside of the loading surface. By adding the gages, the results depicted in Fig. 9 were recovered. The results of this configuration, relative to the result of the corresponding configuration without the extra gage, Fig. 7, are approximately the same. The third rosette in the middle of the flange provides little additional information and is not needed.

The next experiments were done to determine the best placement of the two rosettes on the base of the flange. In the previous trials, the base rosettes were in a set place and were not moved. In Fig. 10, the base rosettes were moved one finite element towards the left. The load recovered is essentially equivalent to the load found in Fig. 6. However, moving the rosettes another element

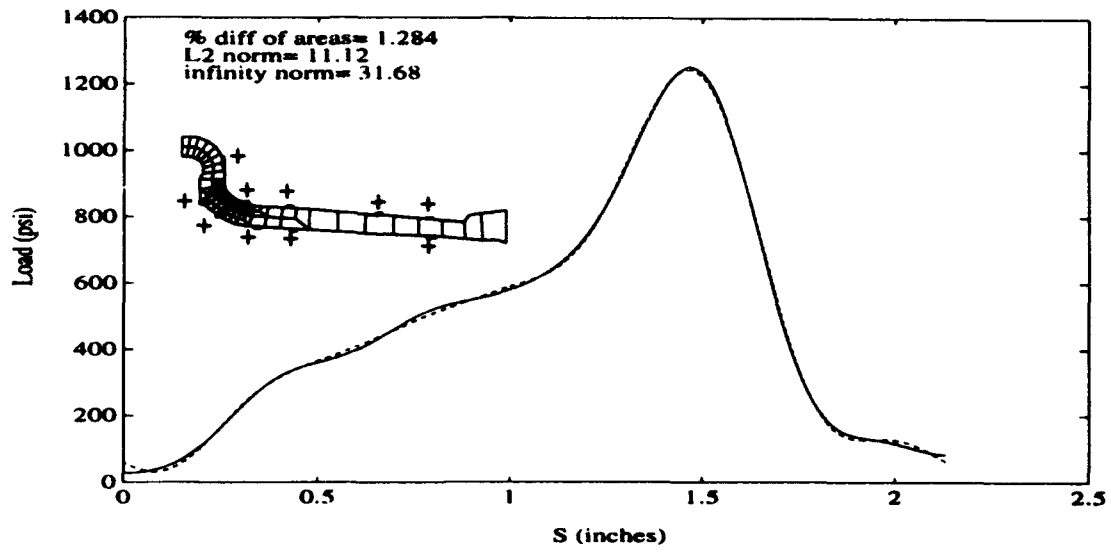


FIGURE 8. Comparison of Analytical and Recovered Load. (--- recovered load, — applied load; Rosettes: 4 out, 3 in, 3 flange)

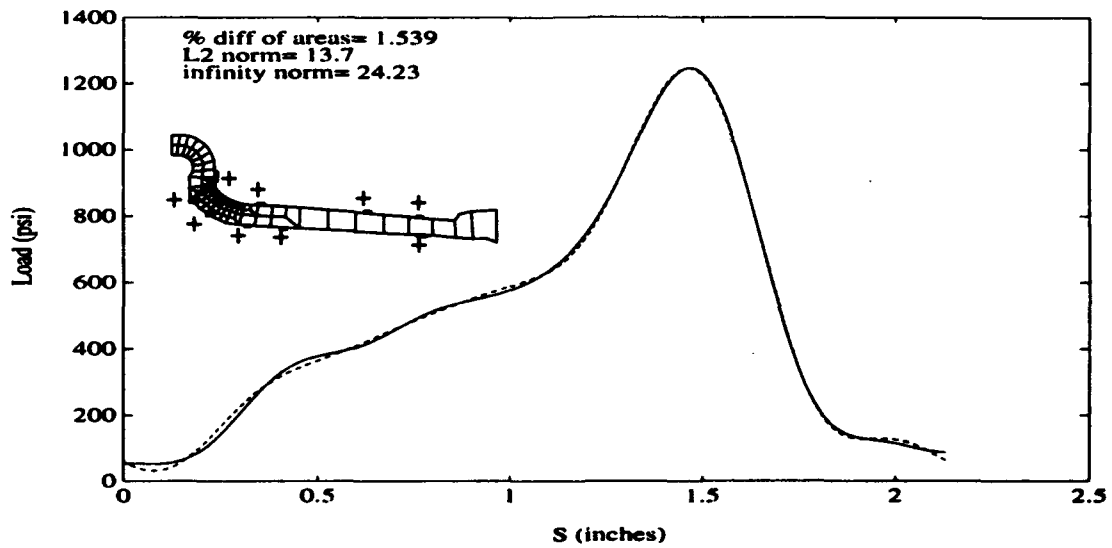


FIGURE 9. Comparison of Analytical and Recovered Load. (--- recovered load, — applied load; Rosettes: 4 out, 2 in, 3 flange)

to the left produced significantly poorer results. It, therefore, was concluded that the configuration in Fig. 6 was the best configuration of rosettes to adequately recover the load.

The previously presented sample problems have been analyzed using the zeroth harmonic in the circumferential direction. The results of other harmonics will now be presented and discussed.

The results for the first, second, and third harmonics are in Figs. 11, 12, and 13, respectively. The results for all three harmonics are comparable to the zeroth harmonic results for the same configuration of strain gages.

Finally, to determine the robustness of the configuration of the strain gages, a different type of load was applied. In this case, the applied load was the mirror image of the previous one. This load is shown as the solid line in Fig. 14. The same configuration of strain gages as used in Fig. 6 is used for the analysis. The analysis was performed for the zeroth mode, and the result is represented by the dashed line in Fig. 14. Although the results are not quite as accurate as those in Fig. 10, it can be concluded that even with a severe modification of the loading, this strain gage configuration allows an accurate recovery of the load.

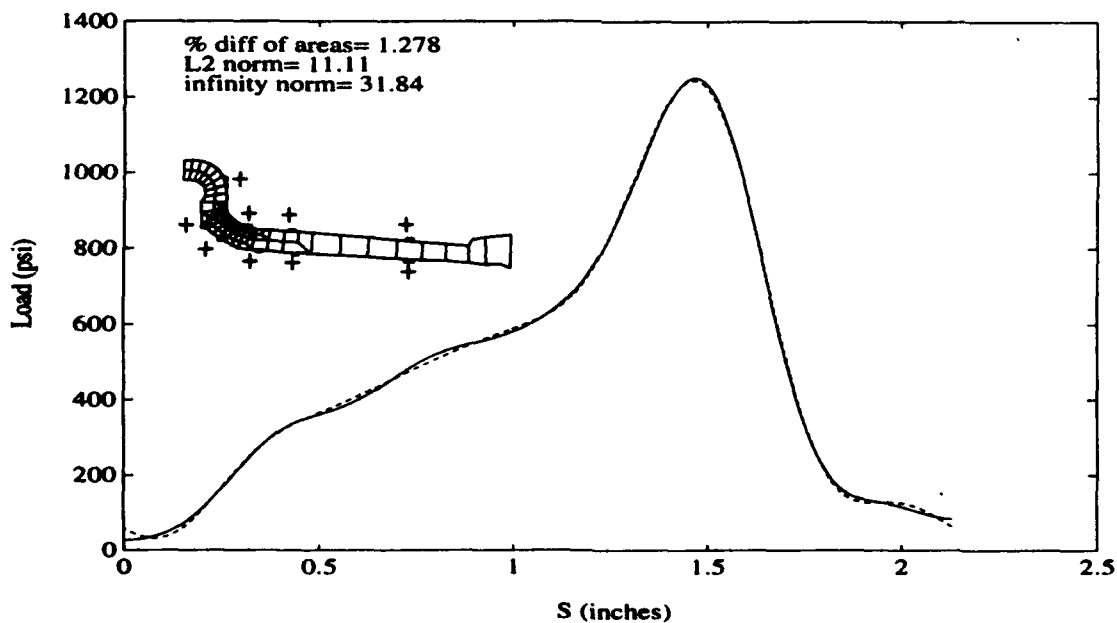


FIGURE 10. Comparison of Analytical and Recovered Load Varying Location on Flange. (--- recovered load, — applied load; Rosettes: 4 out, 3 in, 2 flange)

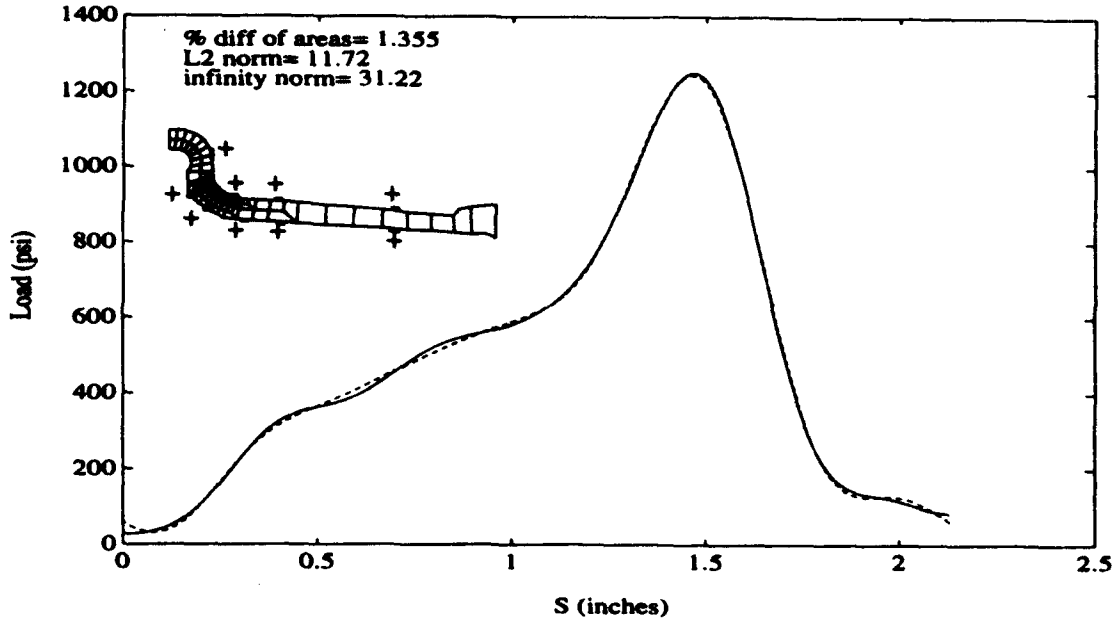


FIGURE 11. Results of ANTWIL for First Mode for Loads Applied and Recovered in the $s(r,z)$ Direction. (--- recovered load, — applied load; Rosettes: 4 out, 3 in, 2 flange)

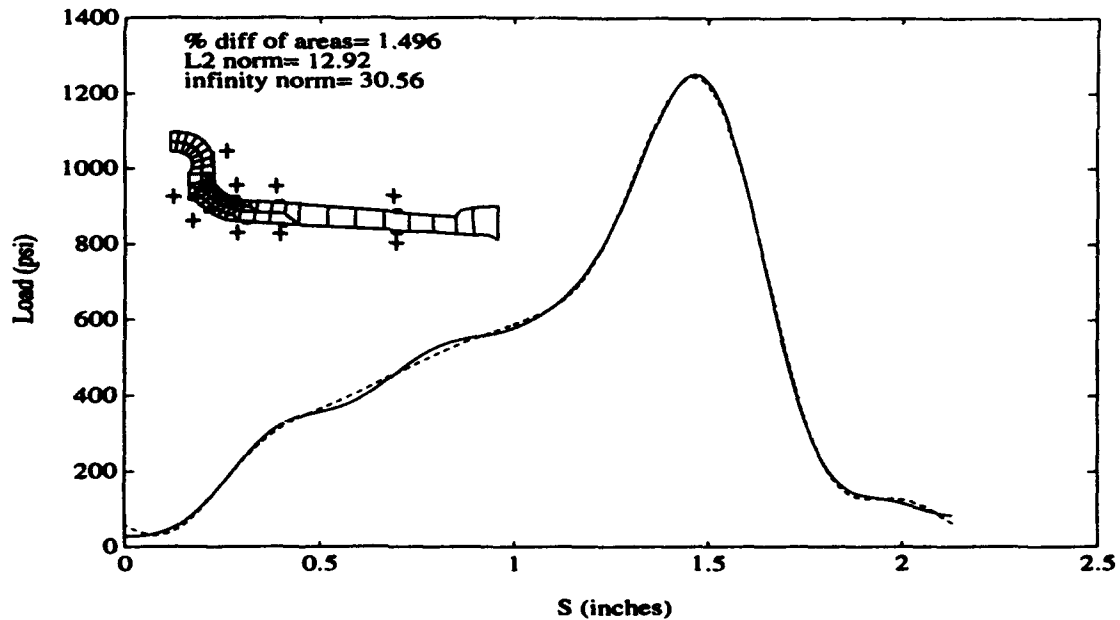


FIGURE 12. Results of ANTWIL for Second Mode for Loads Applied and Recovered in the $s(r,z)$ Direction. (--- recovered load, — applied load; Rosettes: 4 out, 3 in, 2 flange)

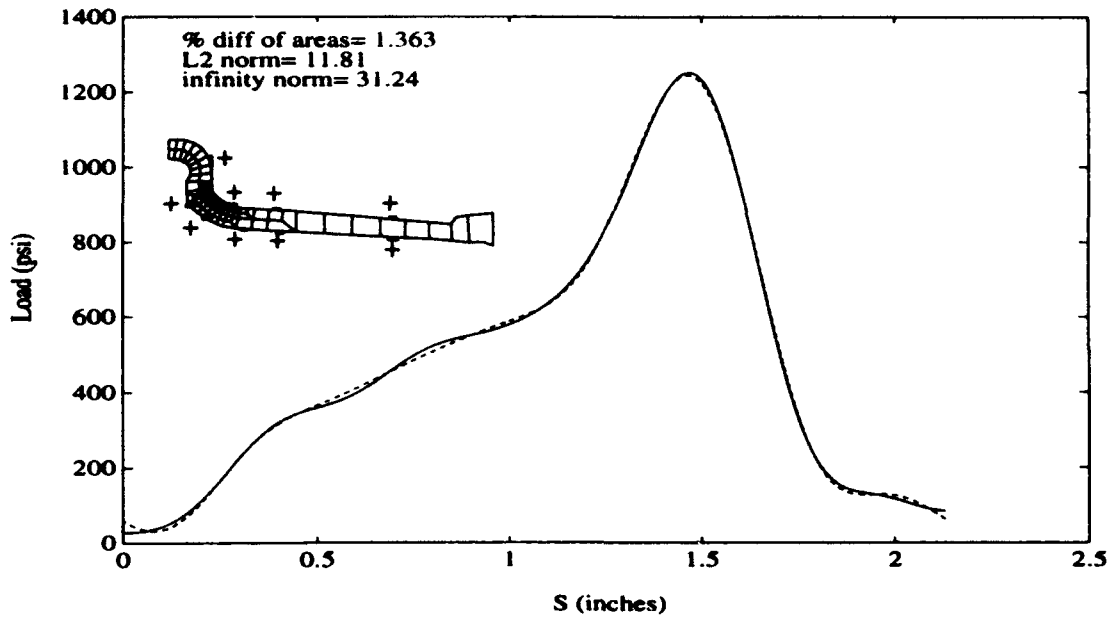


FIGURE 13. Results of ANTWIL for Third Mode for Loads Applied and Recovered in the $s(r,z)$ Direction. (--- recovered load, — applied load; Rosettes: 4 out, 3 in, 2 flange)

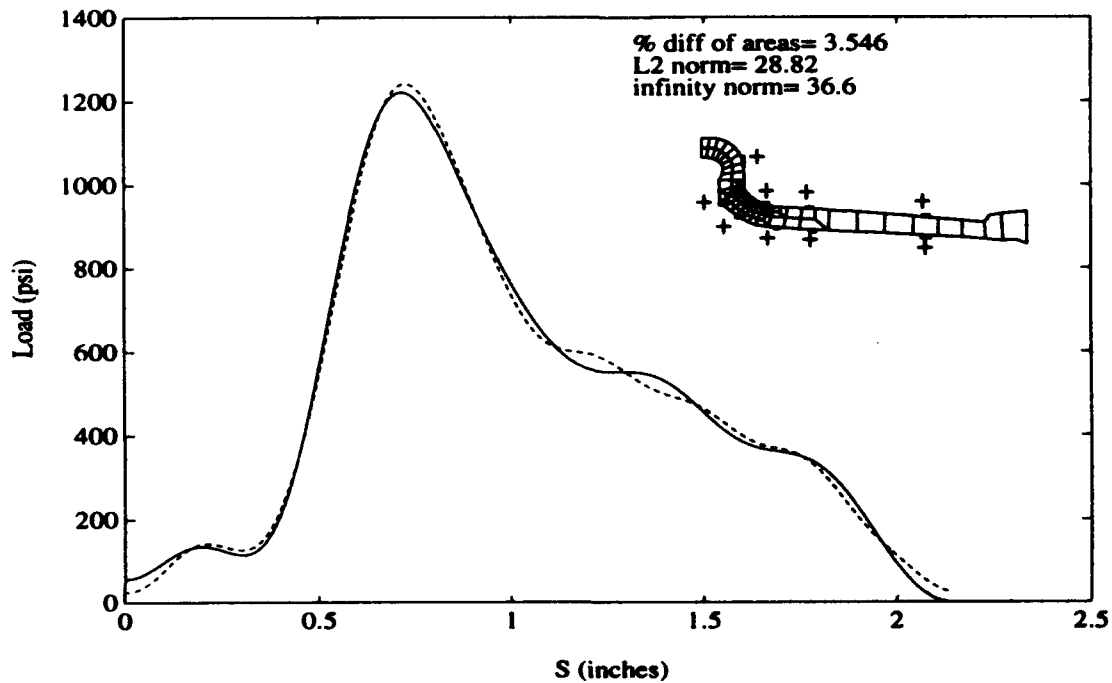


FIGURE 14. Results of ANTWIL for the Mirror Image Load. (--- recovered load, — applied load; Rosettes: 4 out, 3 in, 2 flange)

2.3.2 Block 30 Wheel: Optimal Locations

The various sample problems that were carried out on the Block 30 wheel were helpful in locating the key positions for the strain gages in the bead seat region of the wheel. These positions provide the optimal strain information allowing the algorithm to best capture the tire-wheel interface pressure distribution. Figure 15 and Table 1 illustrate these strain gage locations.

Table 1: Gage Positions^a (F-16 Block 30 Wheel)

Gage(s)	Z -Position (inches)	Side of Flange	Orientation ^b	Distance Along Flange
1	0.6	Tire ^c	Rosette	2.38 inches
2	0.98	Tire	Rosette	
3	1.6	Tire	Rosette	
4	1.68	Outside ^d	Rosette	
5	1.11	Outside	Rosette	
6	0.75	Outside	Rosette	
7	0.39	Outside	Rosette	
8	3.35	Outside	Circumferential	
9	3.35	Tire	Circumferential	

- a. The gages are to be placed in line with a large lightening hole (away from brake lug).
- b. If the orientation is a rosette, place a rosette with middle leg in the z direction from in-board to outboard, i.e., from left to right of Fig. 15.
- c. This side of the flange refers to the side where the bead seat and the tire are placed.
- d. This side of the flange refers to the side opposite from the tire.

2.3.3 Block 40 Wheel

The blue-print of the Block 40 wheel supplied by the Landing Gear Systems Section at Wright-Patterson Air Force Base was used in generating an axisymmetric, eight-node finite element mesh using Patran (see Fig. 16). This mesh was used for the analysis of load recovery at the tire-wheel interface. The Block 30 results were then used as a guide for the initial strain gage placement on the Block 40 wheel. Sample problems for the Block 40 were analyzed by using the zeroth, first, second, and third harmonics in the circumferential direction. The mirror image of the current load was also applied and recovered. These results are presented in this report.

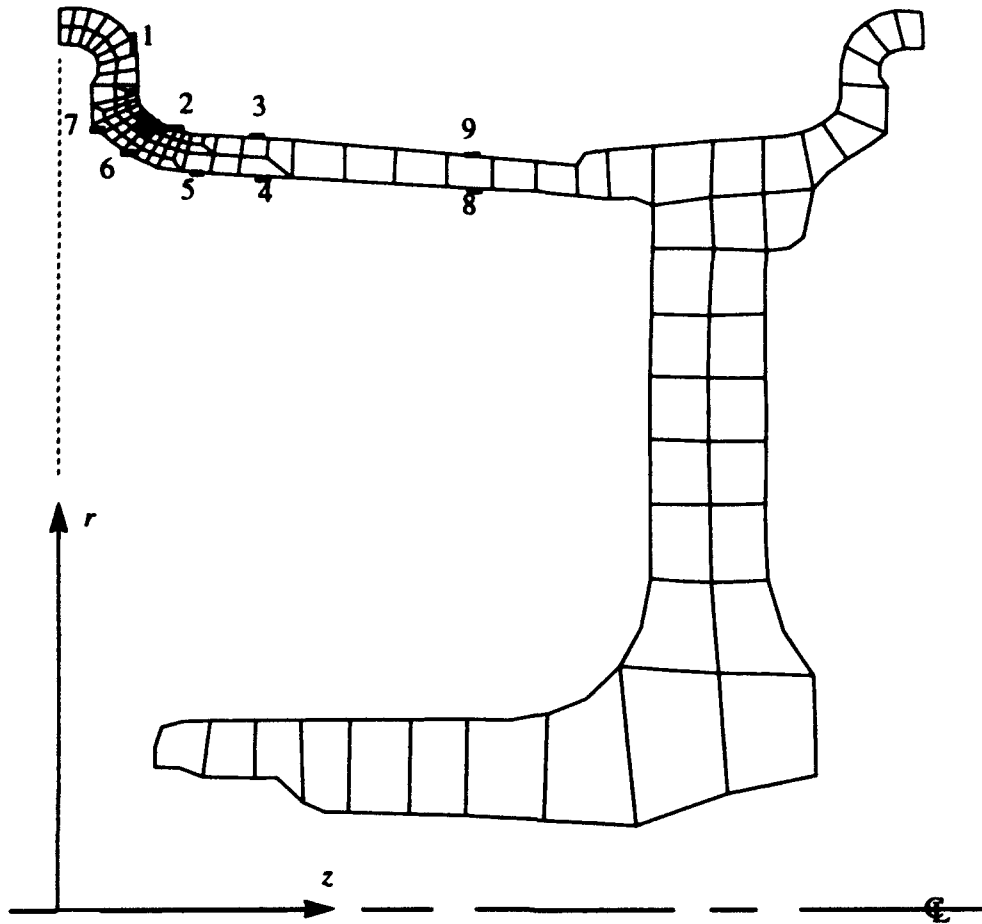


FIGURE 15. Locations of Strain Gages for F-16 Block 30 Wheel.

Using the Block 30 wheel as a model, nine strain gage rosettes were used in the Block 40 test. Seven gages were placed in the bead seat region, three on the tire side, four on the outside. They were spaced to achieve an even distribution along the loading area. The remaining two test points were at the base of the flange, one on the tire side, one on the outside. This configuration returned the load very accurately. Figure 17 shows the applied load and the recovered load along with the error measures employed to assess the effectiveness of the recovery. The two flange area gages were moved toward the bead seat area to determine if the results could be improved, but this was found to have a detrimental effect.

To see if the two gages in the flange area were needed to obtain satisfactory results on the Block 40 wheel, the gages in the flange area were removed entirely, leaving only the seven in the bead seat area. This change also had a deleterious effect. To make up for the information lost

when the two flange gages were removed, an eighth rosette was added on the outside of the bead seat area and the eight gages were again positioned to obtain an even spatial distribution. These results were not quite as good as the first set with the flange gages (see Fig. 18). However, this configuration of eight gages was superior to the nine gage configuration for all the higher harmonics tested. The recovery for harmonics one, two, and three are shown in Figs. 19, 20, and 21. A ninth gage was added to the bead seat area to determine if more information could be gained, but this proved ineffective.

Thus, best configuration is obtained using eight gages, all in the bead seat area. This configuration was also used to successfully recover a mirror image of the modified load for the zeroth, first, second, and third modes. See Figs. 22 through 25.

Based on the results of these studies, Fig. 16 and Table 2 indicate the recommended placement of the eight gages required for satisfactory tire-wheel interface pressure recovery.

Table 2: Gage Positions (F-16 Block 40 Wheel)

Gage(s)	Z -Position (inches)	Side of Flange	Orientation ^a	Distance Along Flange
1	0.73	Tire ^b	Rosette	0.94 inches
2	0.48	Outside ^c	Rosette	
3	0.87	Tire	Rosette	
4	0.72	Outside	Rosette	
5	1.06	Tire	Rosette	
6	0.98	Outside	Rosette	
7	1.61	Tire	Rosette	
8	1.59	Outside	Rosette	
9	2.89	Tire	Circumferential	
10	2.89	Outside	Circumferential	

a. If the orientation is rosette, place a rosette at this position with the middle leg in the z direction from inboard to outboard, i.e., from left to right of Fig 16.

b. This side of the flange refers to the side where the bead seat and tire are placed.

c. This side of the flange refers to the side opposite from the tire.

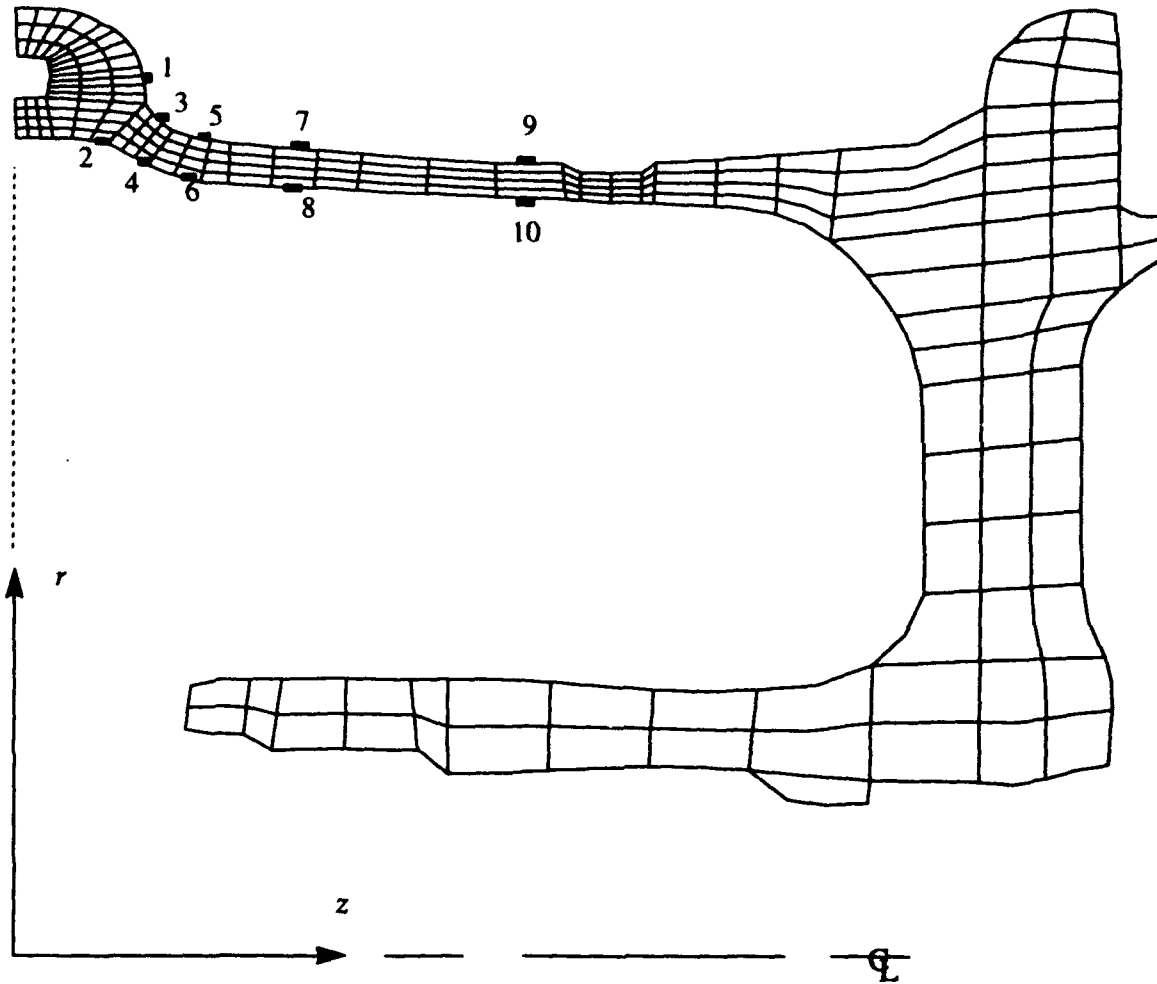


FIGURE 16. Locations of the Optimal Number of Strain Gages for the F-16 Block 40 Wheel.

2.4 Shear Traction

The analytical/experimental algorithm has been extended to include determination of tire-wheel interface shearing tractions, and the ANTWIL finite element code was modified to include this effect. Complex wheel loadings which occur in braking, spin-up, cornering, *etc.*, produce both normal and shear tractions at the tire-wheel interface. The effect of the shear tractions is thought to be important to durability and damage tolerance of the wheel.

The previous coding in ANTWIL was based on calculating nodal loads by using normal components of applied surface tractions. The code has been modified to allow surface tractions of arbitrary orientation. This permits surface tractions with arbitrary normal and shear components. It should be noted that the algorithm given in Section 2.2 applies to the shear traction problem if the pressure $p(\theta, s)$ is taken to be the shear traction. Of course, the finite element load vector

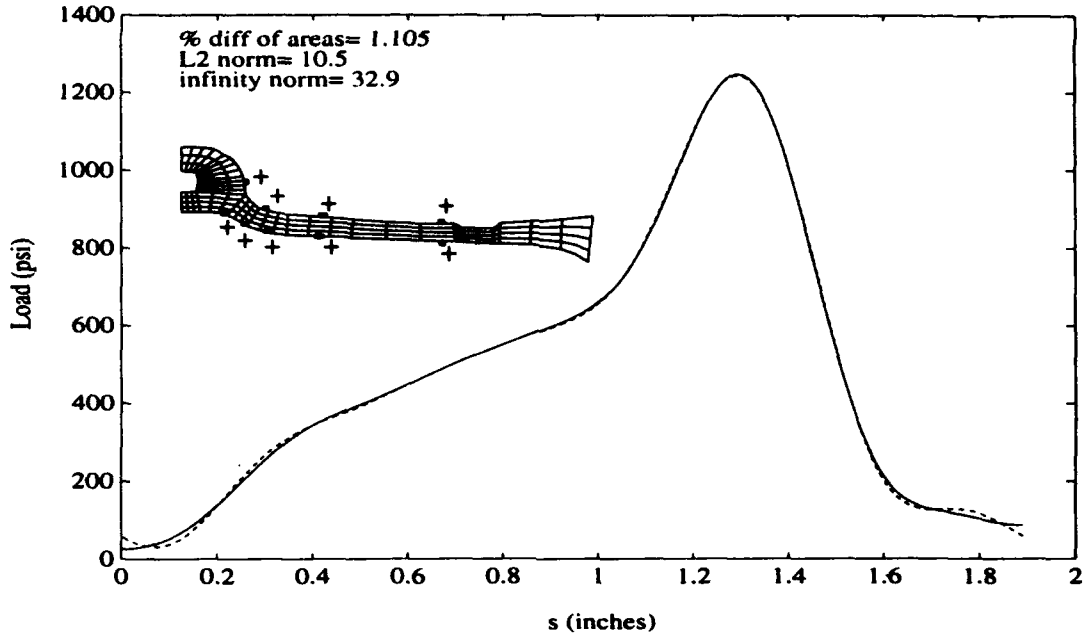


FIGURE 17. Results of ANTWIL for Nine Gage Configuration (--- recovered load, — applied load; Rosettes: 4 out, 3 in, 2 flange)

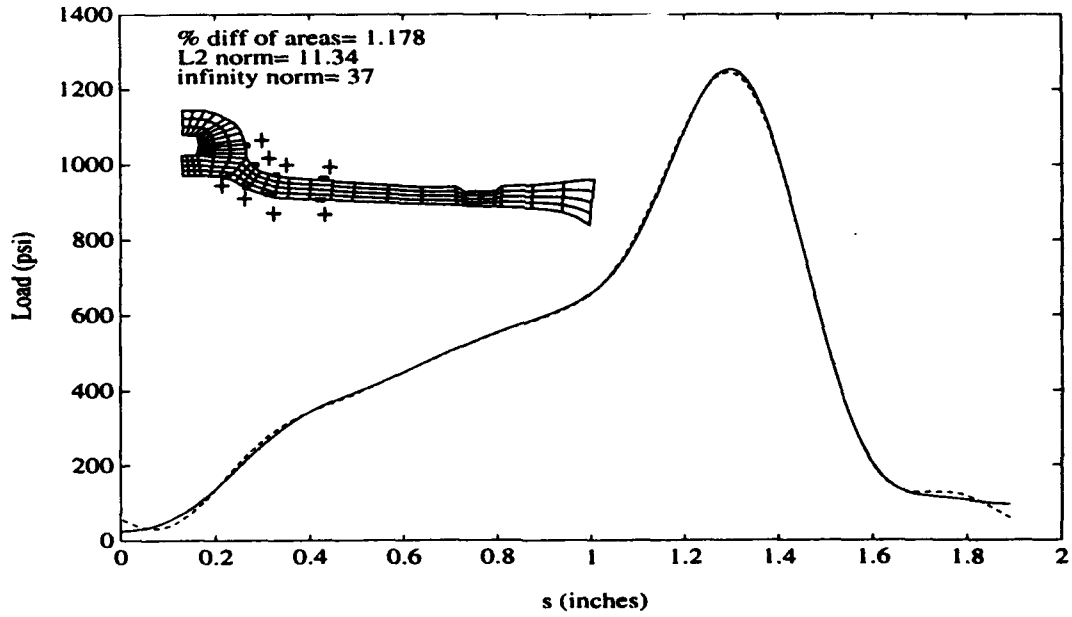


FIGURE 18. Results of ANTWIL for Zeroth Harmonic for Loads Applied and Recovered in the $s(r,z)$ Direction: Eight Gage Configuration (--- recovered load, — applied load; Rosettes: 4 out, 4 in.)

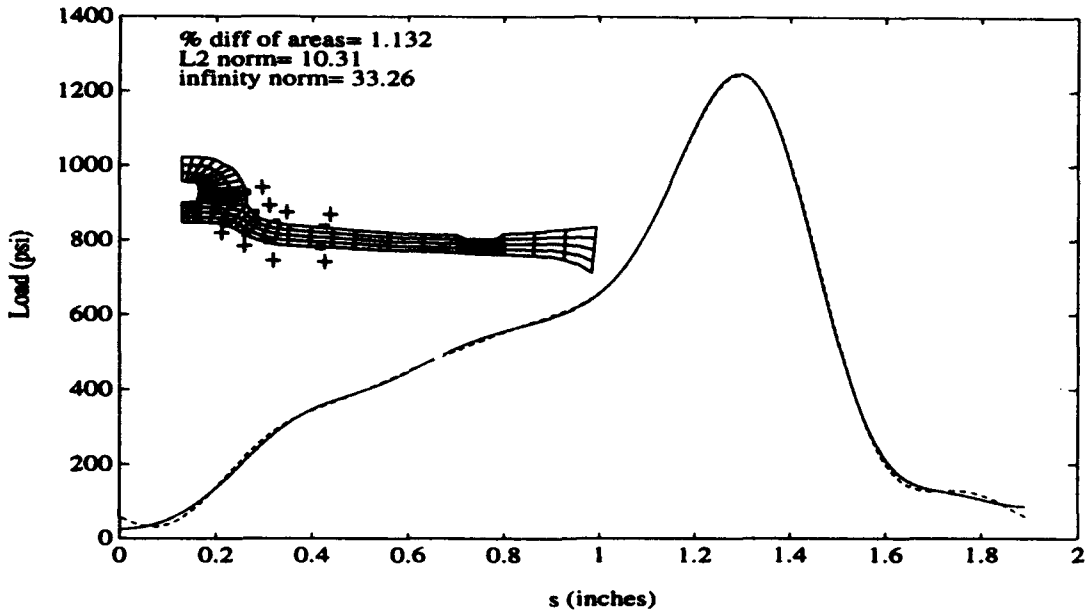


FIGURE 19. Results of ANTWIL for First Harmonic for Loads Applied and Recovered in the $s(r,z)$ Direction: Eight Gage Configuration (--- recovered load, — applied load; Rosettes: 4 out, 4 in.)

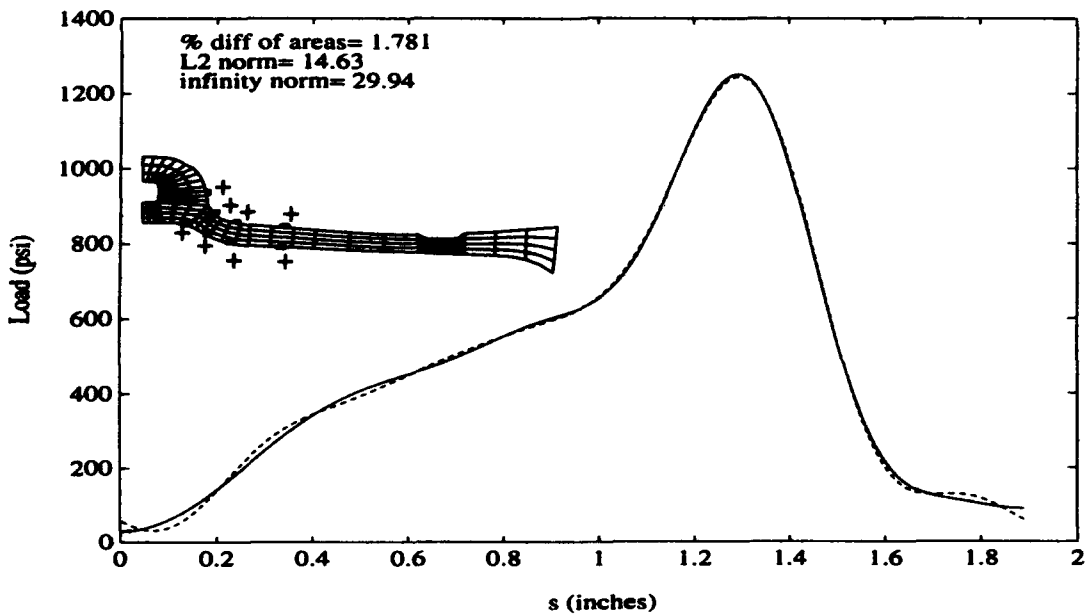


FIGURE 20. Results of ANTWIL for Second Harmonic for Loads Applied and Recovered in the $s(r,z)$ Direction: Eight Gage Configuration (--- recovered load, — applied load; Rosettes: 4 out, 4 in.)

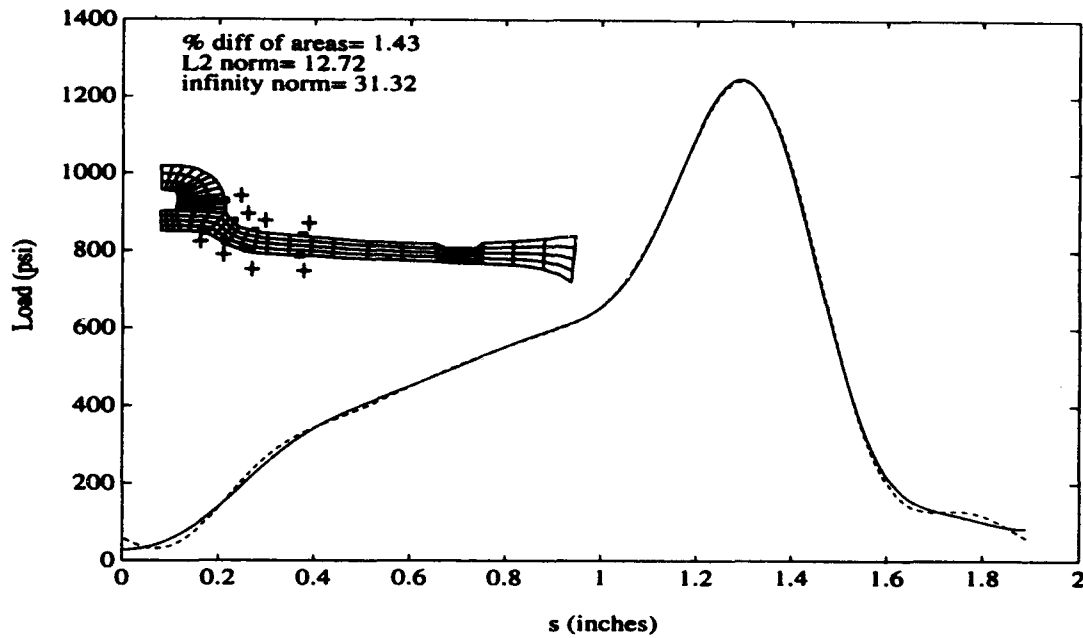


FIGURE 21. Results of ANTWIL for Third Harmonic for Loads Applied and Recovered in the $s(r,z)$ Direction: Eight Gage Configuration (--- recovered load, — applied load; Rosettes: 4 out, 4 in.)

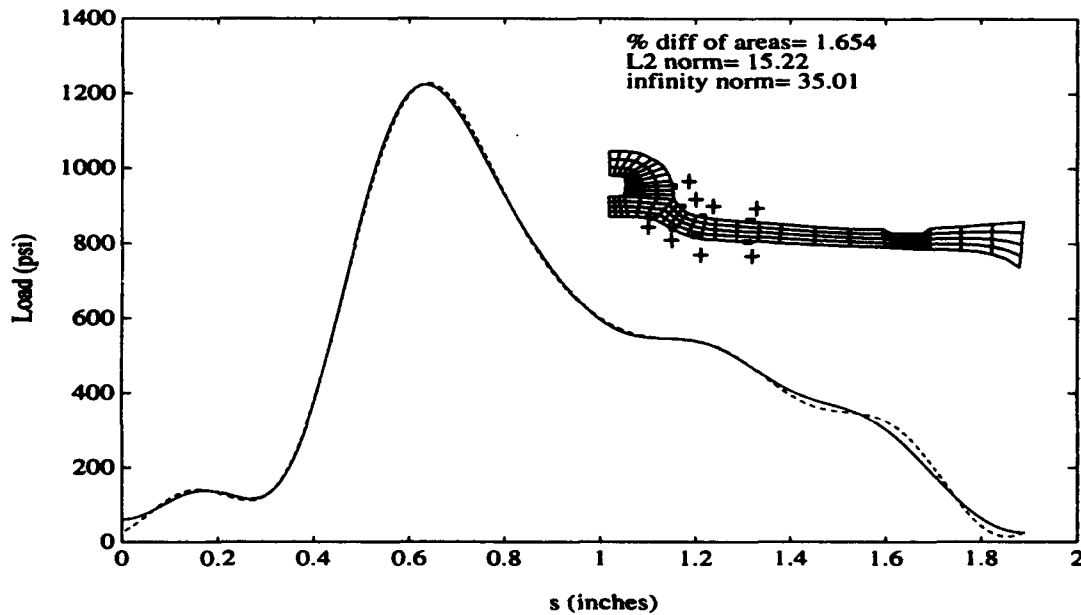


FIGURE 22. Results of ANTWIL for Zeroth Harmonic Using a Mirror Image Load: Eight Gage Configuration (--- recovered load, — applied load; Rosettes: 4 out, 4 in.)

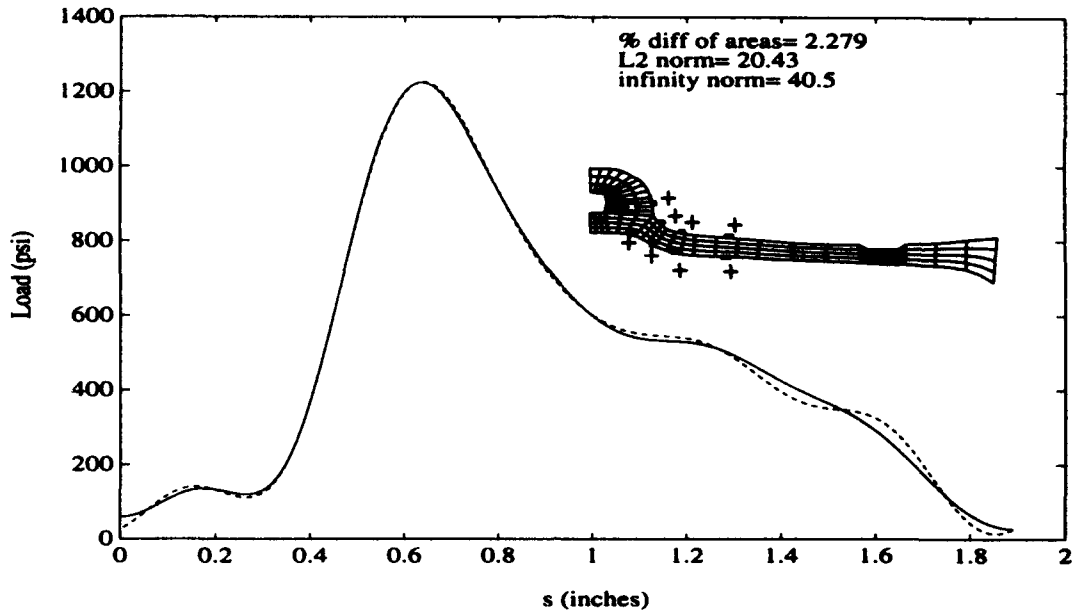


FIGURE 23. Results of ANTWIL for First Harmonic Using a Mirror Image Load: Eight Gage Configuration (--- recovered load, — applied load; Rosettes: 4 out, 4 in.)

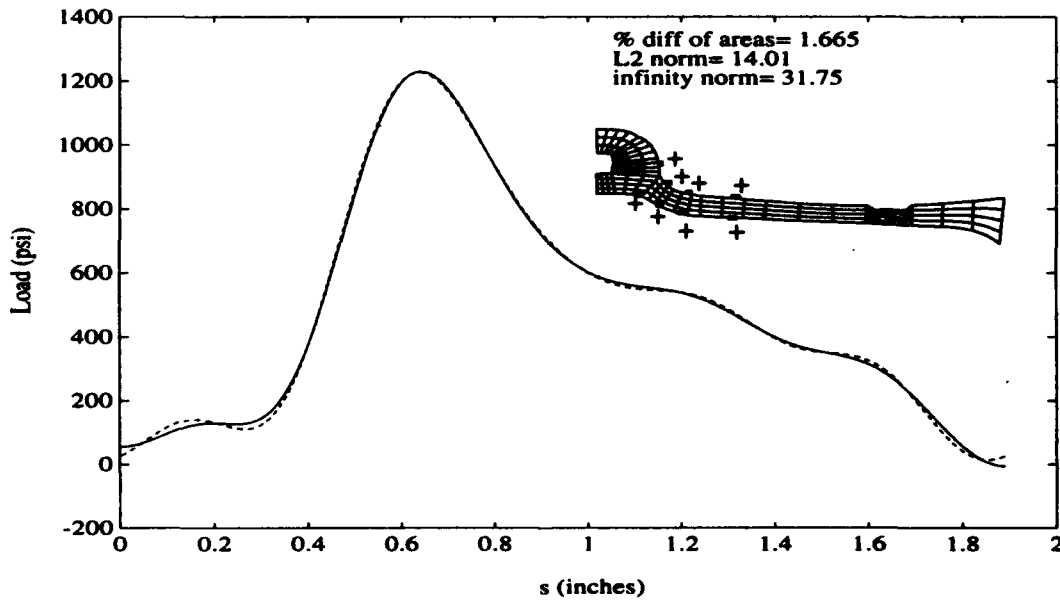


FIGURE 24. Results of ANTWIL for the Second Harmonic Using a Mirror Image Load: Eight Gage Configuration (--- recovered load, — applied load; Rosettes: 4 out, 4 in.)

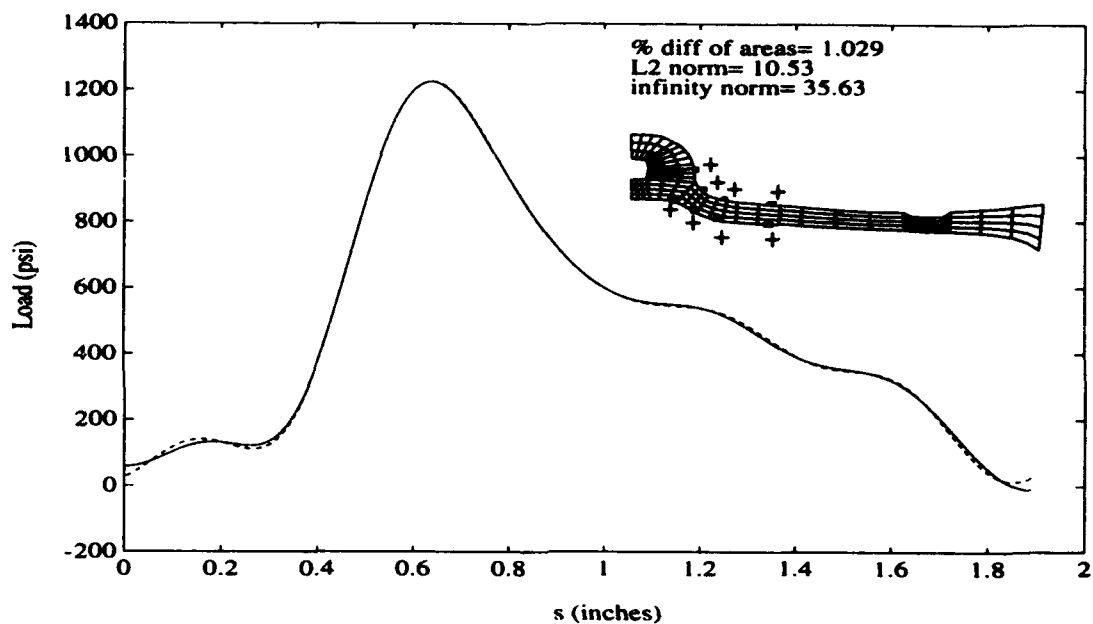


FIGURE 25. Results of ANTWIL for Third Harmonic Using a Mirror Image Load: Eight Gage Configuration (--- recovered load, — applied load; Rosettes: 4 out, 4 in.)

would be assembled accordingly. Several sample problems of shear traction loading have been analyzed to verify the program modifications.

2.4.1 Numerical Experiments.

This research was done to determine if the proposed number and locations of strain gages were adequate to recover tire-wheel interface shear loads. Trials were first done using a simple cylinder in which the exact answer was known. These experiments allowed for a check of the ability of ANTWIL to recover a load in shear and have the model react in an expected way. The cylinder was modeled using a fine and a course mesh, both of which produced similar results, indicating an adequate degree of numerical convergence had been attained. Following these results, trials were run on the Block 30 wheel.

Experiments conducted on the wheel consisted of various loadings, including a constant loading and an assumed variable load. ANTWIL was able to accurately recover these loads. The load employed had the same profile that was applied normal to the surface in previous trials. This load is depicted in Fig. 26. The recovered load is superimposed over the applied load and error norms are given. The figure illustrates the degree to which the program was able to recover the applied load. These results were not as accurate as those achieved in the normal loading. However, the shear loads are usually considered of secondary importance in the determination of the wheel life.

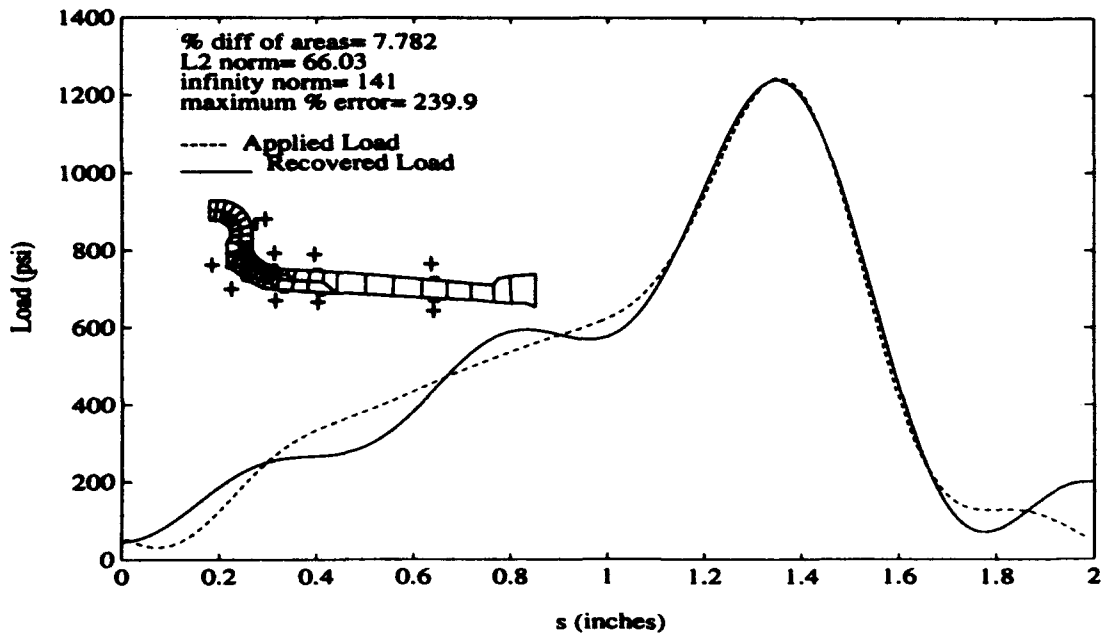


FIGURE 26. Results of ANTWIL: Recovery of Shear Traction
 (--- recovered load, — applied load; Rosettes: 4 out, 3 in, 2 flange)

3.0 Crack Initiation: Literature Review

3.1 Introduction

It is well known that the combination of cyclic stresses due to wheel rotation and corrosive environmental influences can cause surface cracks to form which further enhance stress concentrations leading to crack growth and ultimate failure of the wheel. While current durability and damage tolerance approaches neglect the initiation life of fatigue cracks, this assumption appears to be too conservative for wheel life predictions and needs to be reevaluated in the context of overall life prediction methodology.

A large number of metallurgical observations and numerous experiments have been carried out to understand the basis of crack nucleation. The models formed to understand the process of crack nucleation are based on a wide variety of theories which are both analytical and phenomenological. In the following sections, an effort has been made to separate these models into a few important groups which share a common basis or approach. This review is based primarily on a literature survey performed at WPAFB and with the assistance of WPAFB personnel. The models surveyed can be divided into three principal categories: slip-band theories, continuum damage mechanics theories, and stochastic models. A brief review of this literature including a brief history of the evolution of the models is presented.

3.2 Models Based on Slip Band Theory

According to this theory, the site of crack initiation is often associated with bands of intense slip which are often called persistent slip bands (PSBs). These bands are formed due to the presence of dislocations in the material lattice. The dislocations are caused either due to exclusions or intrusions of foreign particles in the structural matrix.

The first serious study of crack nucleation based on slip band theory was conducted by Thompson, *et al.* [1953]. The experimental studies performed on copper specimens by this group showed that cracks often nucleated at the surface of the material where slip bands were present. In fact, the experiments showed enhanced performance for the specimens in which these persistent slip bands were removed physically, by electro-polishing, during the course of the experiments. There has followed a continuous research effort to investigate the surface nucleation of these slip bands.

Some of the earlier models were based on Mott's assumption [Mott, 1958], that the dislocations moved in different paths in slip bands under cyclic loading. But these models failed to explain the systematic buildup of plastic strain during a cyclic test. Lin and Ito [1969] proposed that one part of the slip band slides in the forward direction and the other part slides in the reverse direction. To make this mode of deformation possible, they assumed a special internal stress field. This theory was largely ignored because it was considered that, in reality, initial stresses were not

present. Since that time, however, researchers (*e.g.*, Brown and Ogin [1985] and Laird [1979]) have established that internal stresses are indeed present. Although the presence of internal stresses in the PSB has been established, there is still some debate as to whether they remain constant or change during cyclic loading, and this has been a major research area for some time. Lin [1985] used the theory of internal stresses in slip bands to estimate the damage accumulated during cyclic loading.

A model based on slip bands was also proposed by Tanaka [1981]. This model differed from previous models by assuming that damage was caused by plastic deformation within the slip band and was modeled by two adjacent layers of dislocation pile ups.

Efforts were also made to investigate the structure and properties of PSBs and their involvement in crack initiation. Mughrabi [1980], and later Brown [1977, 1980], established that PSBs are bands of concentrated slips which essentially carry all the plastic strain in low strain amplitude fatigue test. Some studies also tried to address the issues of the slowing of crack nucleation at grain boundaries and the effects of grain size on the threshold for fatigue crack growth [Ravindran and Dwarkadasa, 1991]. Yoo [1980] conducted a study to investigate twinning and cleavage fracture using a dislocation model. The model was based on the anisotropic elasticity theory of dislocations. High temperature effects in PSBs have also been investigated. Iizuka and Tanaka [1991] investigated temperature effects on stainless steel at 973 K for low cycle fatigue tests.

A different approach was taken by Morris *et al.* [1988]. The model assumed that slip band nucleation and the strain hardening parameters are functions of local plastic flow. The functions incorporated a crack growth equation that was modified for plastic deformation to calculate the cycles required for a microcrack to reach the first subsurface grain boundary when propagating in a region of localized plastic flow.

3.3 Continuum Damage Mechanics Models

Between the microscale (10^{-3} - 10^{-2} mm) and structural (10^2 - 10^3 mm) scale, there exists a macroscale level. The continuum damage mechanics approach deals within that macroscale by defining a damage variable as an effective surface density of cracks or cavity intersections with a plane. Kachanov [1958] used an effective mean stress as a damage variable to model creep rupture. This work was the starting point of other continuum damage models extended to include dissipation and low cycle fatigue in metals by Lemaitre [1971] and coupling between damage and creep by Leckie [1974].

Some of the earliest work on a continuum damage mechanics model for fatigue cracks was carried out by McClintock [1968] and Rice and Tracey [1969]. These models considered defects, *i.e.*, the growth of cavities and microcracks by analyzing their geometry in a continuous matrix

using principles of continuum mechanics. These models explained the phenomenon of crack initiation by means of a micro-mechanics analysis. However, it was recognized that microscale difficulties arise when the analysis has to be applied at a structural scale to predict ductile failures.

Chaboche [1978] provided a continuum thermodynamic foundation to justify the continuum damage mechanics theory. He also studied structural behavior by introducing internal variables to develop a number of phenomenological laws. The formulation adopted three types of internal variables, namely, an isotropic hardening variable, a kinematic hardening variable and a damage variable. The model emphasized the relationship between damage and behavior in deformation. Lemaitre [1985] formulated a model that used effective stress and the laws of thermodynamics to assess damage. The damage in this case was linear with equivalent strain and showed a large influence of triaxial effects through the equivalent stress. However, this model was limited by the hypothesis of isotropy of damage and isotropy of plasticity.

A continuum mechanics model by Tanaka *et al.* [1988] incorporated a recovery effect by diffusion of atoms to explain the initiation of grain-boundary wedge-type cracks in high-temperature fatigue. They assumed that the microscopic direction of deformation is periodically changed in fatigue and that crack initiation was dependent on the deformation history of the grain boundary.

3.3.1 Stochastic Models

Laboratory experiments show that even under identical laboratory conditions and uniform cyclic loading, macroscopically identical metal alloy specimens exhibit large statistical variations in the number of fatigue cycles needed to create a macroscopic crack. It can be argued, therefore, that fatigue failure theory is properly cast as a problem in probabilistic structural mechanics.

Stochastic models in fatigue life prediction have appeared in the literature for some time, primarily devoted to the prediction of crack growth (see Sobczyk and Spencer [1992]). Cox and Morris [1987] formulated a probabilistic model which attempts to link stochastic microstructure and the statistics of measured growth rates. The model is formulated as a semiMarkov processes. The underlying Markov process describes the evolution of a growth control variable as an explicit function of crack length. Elapsed fatigue cycles and the distribution of times of failure are calculated by invoking an empirical or postulated law of growth rate. This law is either a deterministic or probabilistic relationship between the growth control variable and the crack velocity. The model also facilitated the use of spectral loading.

In another paper (Cox, *et al.* [1987]) assumed that the stochastic nature of the short surface - fatigue cracks (on the order of the grain size) under uniform loading may be attributed to their interaction with the stochastic microstructure. In this paper, a computational scheme was proposed to describe the statistical effects of the temporary arrest of short cracks by grain boundaries, and the modification of rates of propagation across grains by various effects of grain boundary

constraint. However, this model was restricted to Mode I (tensile opening) transgranular crack growth under constant amplitude cyclic loading.

The model by Graef [1981], based on slip dislocations, used probabilistic theory to compute the influence of the microscopic inhomogeneity of plastic deformation on initiation of fatigue cracks. A connection between the probability of the occurrence of high surface steps and the number of stress cycles up to crack initiation was noted. He showed that it was possible to calculate the probability of occurrence of initial cracks and to correlate the results of investigations on the first stage of crack propagation in various alloys.

3.3.2 Summary

The models presented in the above summary review several different theories used for understanding crack growth and crack nucleation in metals. It is clear from the literature that a satisfactory approach to the problem of the prediction of crack initiation is still forthcoming. Additionally, the fertile subject of probabilistic mechanics seems not yet to have yielded sufficiently useful results to allow its direct application to crack initiation in aircraft wheels. Also note that the models presented in this review do not include those that are based on continuum fracture mechanics, that is, those that use macroscopically observable parameters to predict crack initiation. These models were largely derived for crack propagation and were later extrapolated to initiation problems.

4.0 Residual Stresses: Literature Review

4.1 Introduction

Mechanical components are often subjected to surface processing treatments to improve mechanical durability. The influence of processes such as shot peening, induction hardening, and carburizing on fatigue performance depends upon the magnitude, distribution, and stability of residual stresses developed during these surface processes. Residual stresses may also develop in service if localized plastic straining occurs. The regions of compressive residual stress are well known to retard fatigue crack growth (or arrest cracks), while tensile residual stress regions produce the opposite effect. However the overall effect of residual stresses on fatigue life is much more complex. For this reason, several experimental and analytical studies have been conducted to understand the behavior of residual stresses on fatigue life. In the following section, a brief review of the current research is presented.

4.2 Residual Stresses: Literature Review

The influence of residual stress on fatigue crack growth has been approached in different ways. Two of the popular approaches are: (a) superposition of the respective stress intensity factors for the residual stress field and for the applied stress, and (b) a crack closure model. Nelson [1982] presented a review of these two approaches with their relative advantages and drawbacks for use in design and analysis. In this paper, only the Mode I crack model was covered.

In the superposition of stress intensity factors, K_I for the residual stress field is obtained by loading the crack faces with the residual stresses which exist normal to the plane of potential crack growth in the uncracked body. Such residual stress intensity factors, K_{res} , have been computed for a number of different crack types and crack face stress distributions (Underwood and Throop, 1979; Grant, 1978). A model based on weight functions was proposed by Parker [1982]. By using weighting functions he tried to predict the crack surface overlapping effects which give rise to nonlinear contact conditions. Further, the weighting functions were used in an iterative process to correct for overlapping effects. The weighting function theory for calculating stress intensity factors in a linear elastic cracked body was introduced by Bueckner [1970].

The effective stress intensity factors are then taken as $K_{eff} = K_{res} + K_{applied}$. The K_{res} is based on elastic analysis. This is the major drawback of this type of analysis as it lacks the ability to account for the influence of possible changes in the residual stress field induced by service loadings before the crack starts and as it grows. Further, most models are only designed to predict growth rate under constant amplitude loading.

The crack closure model has been used to predict load sequence and mean stress effects in specimens with crack-generated residual stress fields. The significance of crack-generated residual stresses was pointed out by Elber [1971], who observed that the residual tensile displacements

left in the wake of a crack would cause it to close before the tensile load was removed and, thus, generate compressive residual stresses in the wake. The crack would not open until a certain level of tensile loading was applied to overcome the crack opening stress resulting from the compressive residual stresses. By correlating crack growth rate with applied mean stress, Elber was able to provide a plausible physical explanation for retardation caused by tensile overloads. This method was further developed by other researchers (Dill and Saff [1976], Budiansky and Hutchinson [1978]) for variable amplitude loadings. The primary disadvantage of this model is that it usually requires an elastic-plastic finite element analysis, which is computationally cumbersome.

A recent paper by Landgraf *et al.* [1988] formulated a stress-based life relationship which incorporated mean stress and residual stress effects to identify the probable failure location (surface or subsurface) and expected fatigue life. In this model, the cyclic properties and behavioral trends developed using axial specimens of steel simulating the various microstructure found in surface treated members have been used to develop a comprehensive procedure for analyzing residual stress effects on fatigue.

Researches have also been conducted on the optimization of surface processing methods and, hence, a control on residual stresses which would provide a better fatigue life. Fuchs [1988] developed a method of analysis for finding optimum shot peening specifications for a given specimen and loading conditions. A simplified analysis showed that the optimum shot peening intensity for a fillet is more than four times the conventionally specified intensity. The effect of elevated temperature on shot peened steel was studied by Childs [1988]. From his experiments, he concluded that a significant portion of the residual compressive stress is lost at very low stresses. He used a hole drilling method to measure the residual stresses. The effect of residual stresses on the morphology of fatigue cracks was investigated by Knowles *et al.* [1991] in a powder-metallurgy 8090 aluminium alloy. Residual stress measurement indicated that the compressive stress levels developed in these materials was significantly greater than in aluminum with conventional metallurgy.

5.0 Summary of Work Performed in FY 92

Following is a summary, by task, of the research performed in FY92.

- **Task I. Improved Experimental Design Methodology.**

Studies have been performed to develop optimal design strategies for determining the tire-wheel interface loads (normal tractions) for landing gear wheels. Although an accurate representation of the tire-wheel interface loads is known to be necessary for durability and damage tolerance analysis of aircraft wheels, these loads are difficult to obtain by either experimental or analytical means. Preliminary research has developed a promising combined analytical/experimental approach to overcome these difficulties. This methodology requires the accumulation of wheel strain gage data as input to the analytical model. However, experience to date indicates that the placement and orientation of the strain gages are crucial to successful performance of the algorithm. Expanding upon initial research efforts, UND has developed a methodology for optimal positioning of the strain gages and for determination of the minimum number of gages for the analysis. In addition to the Block 30 model developed under the previous contract, UND has developed a finite element model of the Block 40 F-16 main landing gear wheel in support of this optimization effort. Specifications for the required number of strain gages and their optimal position for the Block 30 and Block 40 F-16 main landing gear wheels were provided to the directorate at WL/FIVMA to demonstrate the proposed experimental design strategy.

- **Task II. Tire-Wheel Interface Shear Tractions.**

The analytical/experimental algorithm has been extended to include determination of tire-wheel interface shearing tractions, and the ANTWIL finite element code was modified to include this effect. Complex wheel loadings which occur in braking, spin-up, cornering, *etc.*, produce both normal and shear tractions at the tire-wheel interface. The effect of the shear tractions is thought to be important to durability and damage tolerance of the wheel.

- **Task III. Crack Nucleation Modeling and Residual Stress Effects in Aircraft Wheels.**

Preliminary research into models of crack nucleation (initiation), including the effects of residual stresses, has been initiated. The combination of cyclic stresses due to wheel rotation and corrosive environmental influences can cause surface cracks to form which further enhance stress concentrations leading to crack growth and ultimate failure of the wheel. While current durability and damage tolerance approaches neglect the initiation life of fatigue cracks, this assumption appears to be too conservative for wheel life predictions and needs to be reevaluated in the context of overall wheel life prediction methodology. UND will report on the most promising research directions.

6.0 Planned Tasks: FY 93

Given below are the tasks planned for FY 93. A brief description including motivating arguments is given with each task.

- **Task I. Development of a Three-Dimensional Finite Element Model of the Block 30 and Block 50 F-16 Main Landing Gear Wheel**

A fully detailed three-dimensional solid model of the Block 30 and Block 50 F-16 main landing gear wheel will be developed using ARIES [1992]. A preliminary solid model of the Block 30 wheel is shown in Figure 27. The model can then be translated into PATRAN [1988] format. Using this solid model, finite element meshes can be created with arbitrary refinement. That is, the mesh can be modified in areas of high stress gradient, such as the bolt hole region, to an arbitrary degree of refinement. These meshes can be used for a wide variety of verification and analysis studies. The ability to assess the effects of bolt torque will be included in the model. UND will provide the Directorate with the full three-dimensional ARIES solid model, as well as the associated finite element model.

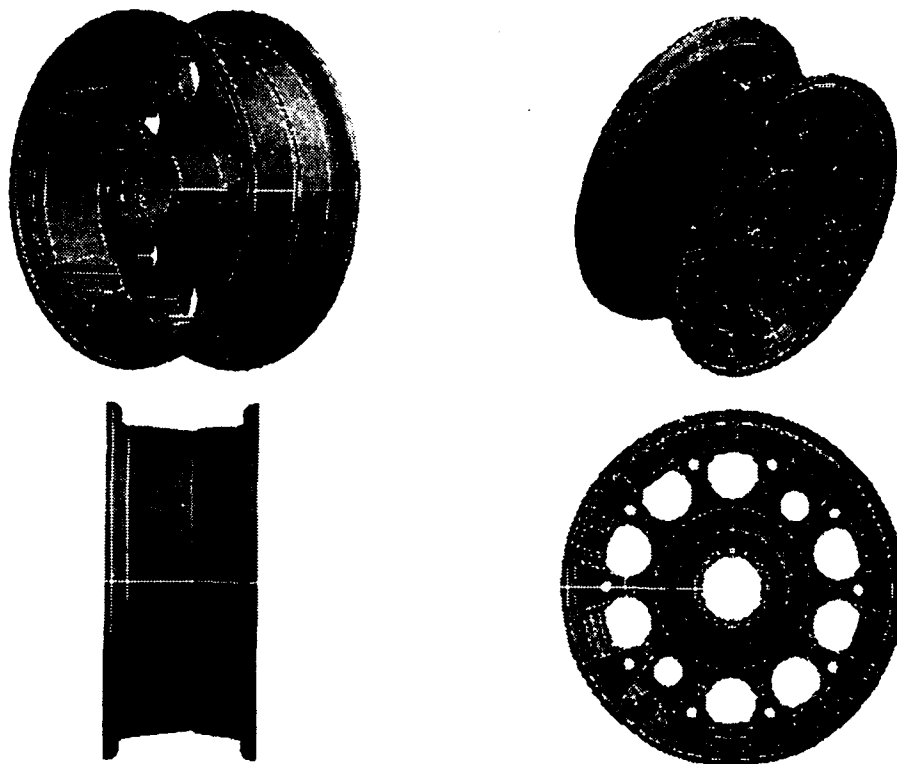


FIGURE 27. Model of F-16 Block 30 Main Landing Gear Wheel

- **Task II. Development of Methods for Applying Tire-Wheel Pressure Distributions to the Three-Dimensional Finite Element Model.**

The tire-wheel interface pressure distribution determined by the combined analytical/experimental procedure developed by UND is essentially an analytical representation of the pressure. That is, the Fortran code, ANTWIL, yields a Fourier series representation of the pressure distribution in the coordinates s and θ where s is a coordinate measuring distance along the wheel flange and θ is the angle giving circumferential location. Likewise, any pressure distributions obtained by a direct measurement technique, recorded digitally or continuously, provide essentially a continuous representation of the interface pressure distribution. In either case, to manually input the values of the pressure distribution on each element surface, as required in a standard three-dimensional finite element code, would be a monumental task and very labor-intensive. This task would have to be repeated for every simulation with a different pressure distribution. Since many computer analyses are anticipated with different pressure distributions, (from different tires, different roll tests, *etc.*) software needs to be developed to make the task of inputting the tire-wheel pressure distribution into a three-dimensional finite element code an automated process. This code should be able to take the required coordinate, nodal point, and element data from ARIES and generate nodal work-equivalent loads. These nodal loads should be output in a file accessible by the user's finite element code or a designated commercially available code such as NASTRAN. Upon completion of this task, the user, given the ARIES generated three-dimensional finite element mesh, can easily perform a sequence of accurate stress analyses for any measured or predicted tire-wheel interface pressure distribution. UND will provide the Directorate with the load generation code and complete documentation including sample analyses. The load generation code will interface with the chosen finite element code given the finite element mesh and analytically or experimentally determined interface pressures.

- **Task III. Verification of Experimentally Determined Pressure Distributions.**

Use of a pressure transducer offers a promising technique for directly measuring tire-wheel interface pressure distributions. Before actual application to the complex tire-wheel problem, the accuracy of any experimental determination should be evaluated by controlled experiments. Thus, tests need to be designed to evaluate the capability of the experimental setup to accurately measure interface pressure distributions. The experimental design should be such that the pressure distribution for the test configuration is precisely known. In addition, the tests should assess the effect on the accuracy of the transducer of (a) in-plane stretching of the transducer that will likely occur during tire mounting and (b) bending of the transducer that occurs when the transducer is mounted in the bead seat region. UND will provide the Landing Gear Section of the Flight Dynamics Directorate with the design of appropriate tests and analytical solutions with which to compare the experimental results.

- **Task IV. Evaluation of Experimental Setup for Tire-Wheel Interface Load Determination.**

Given a positive evaluation of the experimental setup, UND will input the tire-wheel interface pressure distribution obtained from the pressure transducers during wheel roll tests into the three-dimensional finite element model and calculate the resulting strains for comparison to their experimental counterpart. This will provide an assessment of the ability of the experimental setup to perform in realistic situations. Upon successful verification, UND will provide the Landing Gear Section of the Flight Dynamics Directorate with the associated evaluation documentation.

- **Task V. Verification of the Proposed Analytical/Experimental Approach.**

Studies will be performed to verify the proposed analytical/experimental approach for tire-wheel interface load determination for the Block 30 F-16 main landing gear wheels. The Landing Gear Section of the Flight Dynamics Directorate at WL/FIVMA will provide UND with experimental strain survey data for these wheels based upon the experimental design specifications provided in Task I. Tire-wheel interface loads will be extracted from the experimentally obtained strain data using the proposed analytical/experimental algorithm. These loads will then be reapplied to the three-dimensional finite element model of the wheel, and the resulting analytical strains will be compared to their experimental counterpart. In addition, these load profiles will be compared with those obtained from the laboratory experiments. Upon successful completion of this task, UND will provide the Landing Gear Section of the Flight Dynamics Directorate with the verification documentation and the derived load profiles.

- **Task VI. Comparison of Tire-Wheel Interface Pressure Distributions for the Bias Ply and Radial Tires and Their Effect on the Distribution of Wheel Stresses.**

Bias ply and radial ply tires are known to produce different stress distributions on the same wheels. This results in different predictions of wheel service life. WL/FIVMA will perform roll tests with both bias ply and radial ply tires and the strain gage results will be made available to UND. Using the combined analytical/experimental load recovery algorithm implemented in the finite element code ANTWIL, UND will determine the interface pressure distributions. These pressure distributions will be used as input to the three-dimensional finite element model of the wheel developed in Task I. The resulting stress distributions in the wheel will be determined and compared. The comparison will include assessment of the effect of inflation pressure, vertical loads, and yaw. UND will deliver to the Landing Gear Section of the Flight Dynamics Directorate the results of the simulations including a comparative analysis.

- **Task VII. Effect of Bolt Torque on the Distribution of Wheel Stresses.**

The magnitude of the bolt torque is known to have a significant effect on the wheel service life. This undoubtedly affects the stress distribution in critical areas. Given the three-dimensional

finite element model of the wheel generated in Task I and any associated software and the ability to easily perform repeat analyses (Task V), the effects of the bolt torque on wheel stress distribution can readily be studied. UND will provide the Landing Gear Section of the Flight Dynamics Directorate with an analysis of the results of three-dimensional finite element studies performed to assess the effects of different bolt torques.

- **Task VIII. Residual Stress Measurements.**

UND will contract with Lambda Research of Cincinnati, Ohio to make residual stress measurements on the Block 30 F-16 main landing gear wheel at several critical areas and at several depths for inclusion in wheel life assessment. A specific work statement will be written for Lambda Research. UND will keep the Landing Gear Section of the Flight Dynamics Directorate at WL/FIVMA informed of the progress on this task.

- **Task IX. Wheel Fatigue Life Analysis.**

The analytical/experimental approach for determining tire-wheel interface loads will be combined with fatigue and fracture reliability strategies to perform wheel life analyses of aircraft wheels. Both stress-life and fracture mechanics approaches (short and long cracks) will be considered. The effect of residual stresses will be assessed. WL/FIVMA will provide roll-to-failure data to be used in determining possible causes of wheel failure. WL/FIVMA will be provided example analyses for prediction of wheel life. The wheel life predictions for the F-16 Block 30 wheel will include effects of stresses due to bolt torque, inflation pressure, vertical loads, yaw, and residual stresses. UND will also investigate possible design modifications to improve wheel life. A subcontract will be issued to obtain required residual stress measurements for the F-16 Block 30 main landing gear wheel.

7.0 Closure

This report has delineated the accomplishments on the project "Aircraft Wheel Life Assessment" during FY92 and has reviewed the tasks proposed for FY93. Significant progress was made in developing the algorithm for back-calculating tire-wheel interface pressures with the goal of making this a reliable component of the overall life prediction methodology. The ability to take experimental strains, back-calculate the tire-wheel interface pressure and apply the resulting pressure to an accurate, three-dimensional finite element model of the wheel will be totally available sometime during FY93. Complete wheel life assessments, including a comparison of bias ply and radial ply tires, will subsequently be performed.

Additionally, basic literature survey work into the difficult questions of the effects of residual stresses on the wheel life assessment problem and the estimation of the time to crack initiation was begun in FY92. Identification of applicable models incorporating these effects will take place in FY93. This will permit the life estimation methodology to be considerably improved by including these major factors.

8.0 References

- ARIES, ARIES Technology, Inc., Lowell MA, 1992.**
- Barlow, J., "Optimal Stress Locations in Finite Element Models," Int. J. Num. Meth. Engng., Vol. 10, No. 2, 1976, pp. 243-251.**
- Bickford, W. B., A First Course in the Finite Element Method, Richard D. Irwin, Inc., 1990.**
- Brown, L. M., In: Proceedings of the International Conference on the Dislocation Modelling of Physical Systems, Gainesville, Florida, Eds. M. F. Ashby, R. Bullough, C.S. Hartley and J. P. Hirth, 51-68, 1980.**
- Brown, L. M. and Ogin, S. L., "Role of Internal Stresses in the Nucleation of Fatigue Cracks," Fundamentals of Deformation and Fracture, Proceedings of the Eshelby Memorial Symposium, Sheffield, England, April 2-5, 1984, Cambridge Press, 501-528, 1985.**
- Brown, L. M., In Proceedings, Fatigue 1977 conference, Cambridge, U. K. Metal Science, Vol. 11, 315-320, 1977.**
- Bueckner, H. F., "A Novel Principle for the Computation of Stress Intensity Factors," ZAMM 50, 9, 529-546, 1970**
- Budiansky, B. and Hutchinson, J. W., Journal of Applied Mechanics, Transactions of ASME, Vol. 45, pp. 267-276, June 1978.**
- Chaboche, J. L., "Thermodynamic and Phenomenological Description of Cyclic Viscoplasticity with Damage," NTIS N79-30585/0, European Space Agency, Paris.**
- Childs, W. H., "The Effect of Elevated Temperature on Shot Peened 403 Stainless Steel," Analytical and Experimental Methods for Residual Stress Effects in Fatigue, ASTM STP 1004, R. L. Champoux, J. H. Underwood, and J. A. Kapp, Eds., American Society for Testing and Materials, Philadelphia, pp. 21-24, 1988.**
- Cook, R. D., Concepts and Applications of Finite Element Analysis, 3rd Edition, Wiley, 1989.**
- Cox, B. N., and Morris, W. L., "Probabilistic Model of Short Fatigue Crack Growth," Fatigue and Fracture in Engineering Materials and Structures, Vol. 10, 419-428, 1987.**
- Cox, B. N., Pardee, W., and Morris, W. L., "Statistical Model of Intermittent Short Fatigue Crack Growth", Fatigue and Fracture in Engineering Materials and Structures, Vol. 9, 435-455 1987.**
- Dill, H. D. and Saff, C. R., "Fatigue Crack Growth Under Spectrum Loads," ASTM STP 595, American Society for Testing and Materials, pp. 306-319, 1976.**
- Dunham, R. S. and Nickell, R. E., "Finite Element Analysis of Axisymmetric Solids with Arbitrary Loadings", Structural Engineering Laboratory, University of California, Berkeley, California, June 1967.**
- Durup, P. C., and Brussat, T. R., "Wheel Performance Evaluation," FAA Technical Center, 1985**

- Elber, W., "Damage Tolerance in Aircraft Structures," ASTM STP 486, American Society for Testing and Materials, pp. 230-242, 1971.
- Enneking, T. J., "Investigation into the Applicability of Fracture Mechanics Techniques to Aircraft Wheel Life Analysis - Final Report," performed for AFWAL/FIEMA, July 1987.
- Fuchs, H. O., "Approximate Analysis for Optimizing Prestress Treatments," Analytical and Experimental Methods for Residual Stress Effects in Fatigue, ASTM STP 1004, R. L. Champoux, J. H. Underwood, and J. A. Kapp, Eds., American Society for Testing and Materials, Philadelphia, pp. 13-20, 1988.
- Graef, M. "Influence of Microscopic Inhomogeneity of Plastic Deformation on Initiation of Fatigue Cracks," NTIS Number: N82-22531/9, June 1981.
- Grant, A. F., International Journal of Fracture, Vol. 14, No. 4, pp. R221-R229, 1978.
- Iizuka, H. and Tanaka, M., "Effects of grain size on wedge-type crack initiation in low-cycle fatigue at high temperature," Materials at High Temperature, Vol. 9, 17-22, Akita University, Akita, Feb 1991.
- Kachanov, L. M., "Time of the Rupture Process Under Creep Conditions," Introduction to Continuum Damage Mechanics, Martinus Nijhoff Publishers, The Netherlands, 1986.
- Kandarpa, S. Spencer, B. F., Jr. and Kirkner, D. J., "Determination of Tire - Wheel Interface Loads," WL-TR-91-3102, Flight Dynamics Laboratory, Wright Research and Development Center, Wright-Patterson Air Force Base, Ohio. 1991.
- Knowles, D. M. and King, J. E., "Influence of Microscopic Residual Stress Fields on Fatigue Crack Growth Measurements in SiC Particulate reinforced 8090 aluminium alloy," Material Science and Technology, Vol. 7, pp. 1015-1020, Nov. 1991
- Laird, C. Proceedings of the A.S.M. Materials Science Seminar, St. Louis, Missouri, 149-203, 1979.
- Landgraf, R. W. and Chernenkoff, R. A., "Residual Stress Effects on the Fatigue of the Surface Processed Steels," Analytical and Experimental Methods for Residual Stress Effects in Fatigue, ASTM STP 1004, R. L. Champoux, J. H. Underwood, and J. A. Kapp, Eds., American Society for Testing and Materials, Philadelphia, pp. 1-12, 1988.
- Lawler, W. T., Spencer, B. F., Jr. and Enneking, T. J., "Damage Tolerance of Aircraft Wheels," WRDC-TR-89-3109, Flight Dynamics Laboratory, Wright Research and Development Center, Wright-Patterson Air Force Base, Ohio.
- Leckie, F., and Hayhurst, D., "Creep Rupture of Structures," Proceedings of Royal Society. London, Vol. 240, 323-, 1974.
- Lemaitre, J., "Evaluation of Dissipation and Damage in Metals Submitted to Dynamic Loading," Proceedings I.C.M. I, Kyoto, Japan, 1971.

- Lemaitre, J., "A Continuous Damage Mechanics Model for Ductile Fracture," *Journal of Engineering Materials and Technology*, Vol. 107, 83-89, January 1985.
- Lin, T. H., and Ito, Y. M., "Mechanics of Fatigue Crack Nucleation Mechanism," *Journal of the Mechanics and Physics of Solids*, Vol. 17, 511-523, 1969.
- Lin, M -R., "Experimental and Theoretical Study of fatigue Crack Initiation in Metals," Dissertation, MA Number: 85-314413, June 1985.
- McClintock, F., "A Criterion for Ductile Fracture by the growth of Holes," *ASME Journal of Applied Mechanics*, June 1968.
- Mott, N. E., "A Theory of the Origin of Fatigue Cracks," *Acta Metallurgica*, Vol. 6, 195-197, 1958.
- Morris, W. L., James, M. R., and Cox, B. N., "Fatigue Crack Initiation Mechanics of Metal Aircraft Structures", NTIS AD-A210 567/4/XAB, Aug 1988.
- Mughrabi, H., "Microscopic Mechanisms of Metal Fatigue," Fifth International Conference on the strength of Metals and Alloys, Aachen, Eds. P. Haasen, V. Gerold and G. Kastorz, Vol. 3, 1615-1638, Pergamon Press, New York, 1980.
- Nelson, D. V., "Effects of Residual Stress on Fatigue Crack Propagation," *Residual Stress Effects in Fatigue*, ASTM STP 776, American Society for Testing and Materials, pp. 172-194, 1982.
- Parker, A. P., "Stress Intensity Factors, Crack Profiles, and Fatigue Crack Growth Rates in Residual Stress Fields," *Residual Stress Effects in Fatigue*, ASTM STP 776, American Society for Testing and Materials, pp. 13-31, 1982.
- PATRAN, PDA Engineering, Costa Mesa CA, 1988.
- Ravindran, K. S. and Dwarkadasa, E. S., "Theoretical modelling of the effects of the grain size on the threshold for fatigue crack growth," *Acta Metallurgica et Materialia*, Vol. 39, 1343-1357, June 1991.
- Rice, J., and Tracey, D., "On Ductile Enlargement of Voids in Triaxial Stress Fields," *Journal of Mechanics Physics of Solids*, Vol. 17, 1969.
- Sobczyk, K., and Spencer, B. F., "Random Fatigue: From Data to Theory," Academic Press, New York, 1992.
- Tanaka, Manabu, Iizuka, Hiroshi, "A Micro-mechanics Model of the Initiation of Grain-Boundary Crack in High-Temperature Fatigue," *Low Cycle Fatigue*, ASTM, 611-621, 1988.
- Tanaka, K. and Mura, T., "A Dislocation Model for Fatigue Crack Initiation," *Journal of Applied Mechanics*, Vol. 48, 97-103, 1981.
- Timoshenko, S. P. and Goodier, J. N., *Theory of Elasticity*, 3rd Edition, McGraw-Hill, 1970.
- Thompson, N. et al., *Philosophical Magazine*, Vol. 1, 113-115, 1953.

- Treanor, D. and Boike, M. R., "Military Aircraft Wheel Load Spectrum Development," Flight Dynamics Laboratory, Wright Research and Development Center, WRDC-TR-3109, Wright-Patterson Air Force Base, Dec. 1988.
- Treanor, D. and Carter, T. J., "Military Aircraft Wheel Life Improvement Assessment," Air Force Wright Aeronautical Laboratories, Flight Dynamics Lab, 1987.
- Underwood, J. H. and Throop, J. F. "Part-Through Crack Fatigue Life Predictions," ASTM STP 687, American Society for Testing and Materials, pp. 195-210, 1979.
- Yoo, M. H., "A dislocation model for twinning and fracture and its application to HCP metals," Proceedings of Fifth International Conference, Aachen, West Germany, August 27-31, 1979, Vol. 2, Pergamon Press, 825-830, 1980.

Appendix A- Finite Element Formulation

This appendix will present the concepts of finite element modeling which are used for analysis of axially symmetric bodies. A mathematical model for axially symmetric bodies is described. The loading, which is not axially symmetric, is also discussed. Loads which are asymmetric are solved by superposition of results obtained from the components of Fourier series.

Introduction

An axisymmetric solid can be thought of as a solid generated by revolving an area in the rz plane around the z axis, as indicated in Figure A-1. The solid body which is generated in this manner will be geometrically axially symmetric, and if the material properties, loads and support conditions are also axially symmetric (*i.e.*, the variation is independent of the θ direction), then the static problem will have displacements and stresses which are independent of θ . This essentially means that the problem is mathematically two-dimensional, where displacements are defined in only the radial and axial directions. The analysis procedure for such a problem is similar to that of plane strain or plane stress.

In most cases of interest, however, the solid of revolution is subjected to a loading which is not axially symmetric, or the material property may not be isotropic. In either case, the displacements and the stresses are no longer two-dimensional but three-dimensional. An asymmetric loading can be represented by a Fourier series, and the analysis is done for each load component. Then using the principle of superposition, the original problem is solved by adding the solutions of the

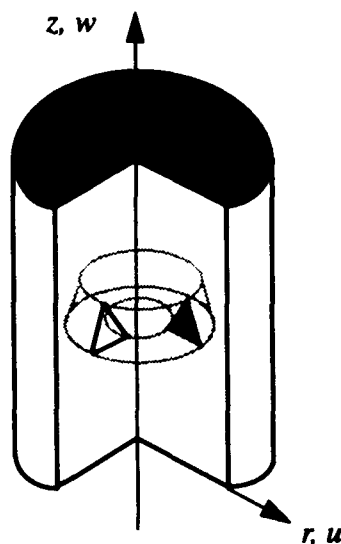


FIGURE A-1. Axisymmetric Body with Triangular Elements.

component problems. Thus, a three-dimensional problem is broken into a series of two-dimensional problems. In most cases solving the problem by a series of two-dimensional components has proved to be fruitful as compared to a full three-dimensional solution, especially in terms of memory allocation and computational time. Besides, three-dimensional problems are difficult to set up and run.

Formulation

The finite element method for linear elastic stress analysis can be derived by many techniques. The approach taken, herein, is to use the principle of virtual displacements.

The strain-displacement relationship for a linear elastic material can be written as:

$$\boldsymbol{\epsilon} = \mathbf{L}\mathbf{U}, \quad (25)$$

where $\boldsymbol{\epsilon}$ = vector of strains, \mathbf{L} = matrix operator which defines the strains in terms of the displacements, and \mathbf{U} = vector of displacements. The stress-strain relation is given by the following expression:

$$\boldsymbol{\sigma} = \mathbf{D}(\boldsymbol{\epsilon} - \boldsymbol{\epsilon}_o) + \boldsymbol{\sigma}_o, \quad (26)$$

where $\boldsymbol{\epsilon}_o$ = vector of initial strains, $\boldsymbol{\sigma}_o$ = vector of residual or initial stress, and \mathbf{D} = elasticity matrix which depend upon the properties of the material.

A virtual displacement $\delta\mathbf{U}$, which belongs to a class of admissible functions, is imposed on the system and the external work is equated to the internal work and integrated over the entire volume of the system. This relationship is expressed as:

$$\int_V (\delta\boldsymbol{\epsilon}^T \boldsymbol{\sigma}) dV = \int_V (\delta\mathbf{U}^T \mathbf{b}) dV + \int_A (\delta\mathbf{U}^T \mathbf{q}) dA, \quad (27)$$

where \mathbf{b} = vector of body forces per unit volume, and \mathbf{q} = vector of surface tractions acting over a surface A .

The formulation of the basic equations can be done at the element level where the equations are summed for each element over the entire continuum. To reduce the problem to finite dimensions, the displacements within each element are interpolated from nodal displacements. This relation is given by the following expression:

$$\mathbf{U} = \mathbf{N}\mathbf{a}, \quad (28)$$

where \mathbf{a} = vector of nodal displacements, and \mathbf{N} = matrix of interpolation functions or shape functions. Substituting Equation (28) into Equation (25), the approximate strain-displacement relationship is given by:

$$\hat{\epsilon} = \mathbf{B}\mathbf{a}, \quad (29)$$

where:

$$\mathbf{B} = \mathbf{L}\mathbf{N}, \quad (30)$$

and, $\hat{\epsilon}$ = approximate strain vector. On substituting Equation (28) and Equation (30) into Equation (27), the virtual work expression becomes:

$$\int_V (\mathbf{B}\delta\mathbf{a})^T \{ \mathbf{D}(\mathbf{B}\mathbf{a} - \epsilon_o) + \sigma_o \} dV = \int_V (\mathbf{N}\delta\mathbf{a})^T \mathbf{b} dV + \int_A (\mathbf{N}\delta\mathbf{a})^T \mathbf{q} dA + \delta\mathbf{a}^T \mathbf{P} \quad (31)$$

Rearranging Equation (31) and assuming that virtual displacement, $\delta\mathbf{a}$, is not equal to zero, the above expression can be written as:

$$\mathbf{K}\mathbf{a} = \mathbf{f}, \quad (32)$$

where K = stiffness matrix given by,

$$\mathbf{K} = \int_V (\mathbf{B}^T \mathbf{D} \mathbf{B}) dV, \quad (33)$$

and \mathbf{f} = vector of loading components due to the body forces, traction forces, concentrated forces and residual stresses and strains. Further it can be expressed as:

$$\mathbf{f} = \int_V (\mathbf{N}^T \mathbf{b}) dV + \int_A (\mathbf{N}^T \mathbf{q}) dA + \int_V (\mathbf{B}^T \mathbf{D} \epsilon_o) dV + \int_V (\mathbf{B}^T \sigma_o) dV + \mathbf{P}, \quad (34)$$

where \mathbf{P} = point load vector acting at the nodes.

Axisymmetric Body with Asymmetric Loading

As alluded to earlier, axisymmetric solids may have loads which may or may not be axially symmetric. The situation in which loading is asymmetric can be solved by decomposing the loading function using a Fourier series in the θ -direction and superposing the results. The body will have deformations in the r , θ and z directions. In fact, the symmetric case can be seen as a special case of the above, by having only the zeroth component of the Fourier series (Figure A-2a) where the displacements are only in the r and z direction. Thus, a mathematical model for the most general case can be developed which incorporates the special case of symmetric loading.

Let the loading on the body be expressed as a Fourier series, which can be written as [Cook, 1977]:

$$[Q_r, Q_z, S_r, S_z, T] = \sum_n L_{nc}^s \cos(n\theta) + \sum_n L_{ns}^a \sin(n\theta) \quad (35)$$

$$[Q_\theta, S_\theta] = \sum_n L_{ns}^s \sin(n\theta) + \sum_n L_{nc}^a \cos(n\theta) \quad (36)$$

where Q's and S's are vectors of body forces and surface tractions in the r , θ and z directions and T = vector of temperatures. L contains the amplitudes of the vectors of body forces and surface tractions. L_{nc}^s and L_{ns}^a are the cosine and sine amplitudes and represent a state of

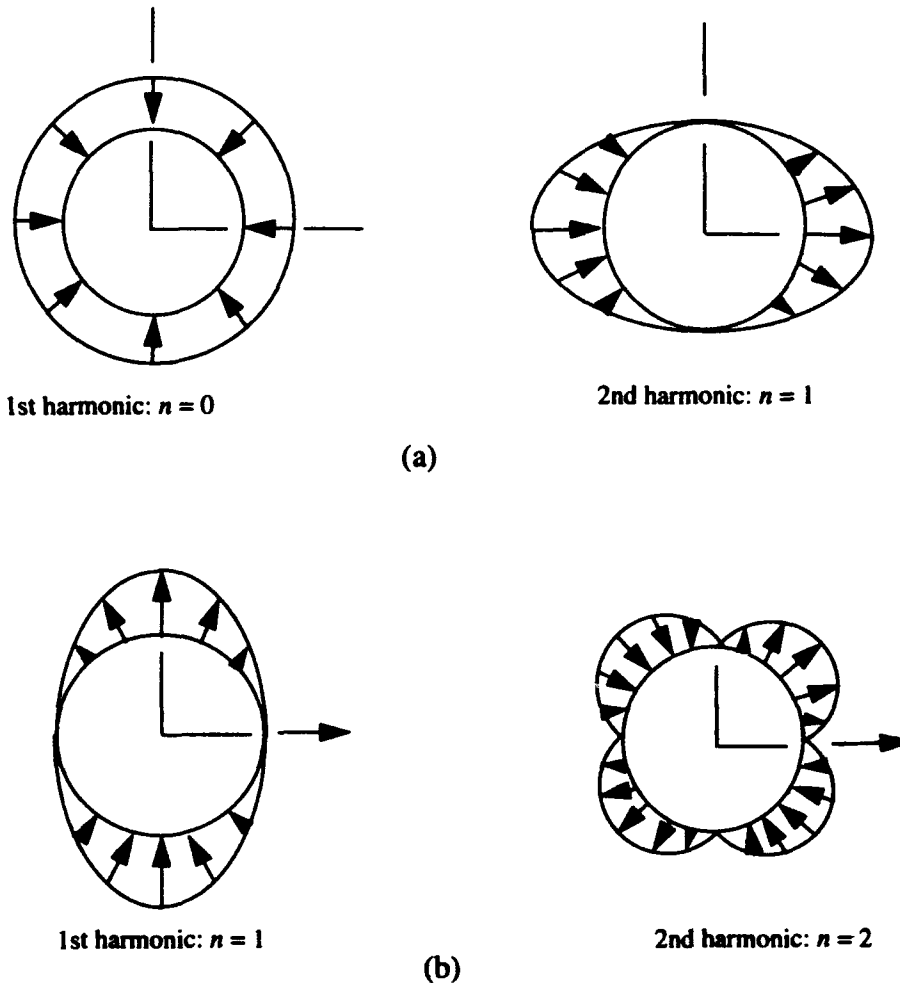


FIGURE A-2. (a) Symmetric Loads with Respect to $\theta = 0$ Due to Cosine Terms. (b) Asymmetric Loads with Respect to $\theta = 0$ Due to Sine Terms.

symmetry with respect to the plane $\theta = 0$, where as L_{ns}^a and L_{nc}^a are the sine and cosine amplitudes for the antisymmetric case. These equations can be expressed as:

$$L_{nc}^s = [Q_{rn}^s, Q_{zn}^s, S_{rn}^s, S_{zn}^s, T_n] \quad (37)$$

$$L_{ns}^s = [Q_{\theta n}^s, S_{\theta n}^s] \quad (38)$$

$$L_{nc}^a = [Q_{rn}^a, Q_{zn}^a, S_{rn}^a, S_{zn}^a, T_n^a] \quad (39)$$

$$L_{ns}^a = [Q_{\theta n}^a, S_{\theta n}^a] \quad (40)$$

It can be shown [Cook, 1977] that under the above loadings the displacements have the following form:

$$\mathbf{u} = \sum_n \mathbf{u}_n^s \cos(n\theta) + \sum_n \mathbf{u}_n^a \sin(n\theta) \quad (41)$$

$$\mathbf{v} = \sum_n \mathbf{v}_n^s \sin(n\theta) - \sum_n \mathbf{v}_n^a \cos(n\theta) \quad (42)$$

$$\mathbf{w} = \sum_n \mathbf{w}_n^s \cos(n\theta) + \sum_n \mathbf{w}_n^a \sin(n\theta) \quad (43)$$

where \mathbf{u} = radial displacement, \mathbf{v} = circumferential displacement and \mathbf{w} = axial displacement.

The strain-displacement or the kinematic relation which is given in Equation (26) is expressed here in cylindrical coordinates:

$$\begin{bmatrix} \epsilon_r \\ \epsilon_\theta \\ \epsilon_z \\ \gamma_{zr} \\ \gamma_{r\theta} \\ \gamma_{\theta z} \end{bmatrix} = \begin{bmatrix} \partial/(\partial r) & 0 & 0 \\ 1/r & \partial/(r\partial\theta) & 0 \\ 0 & 0 & \partial/(\partial z) \\ \partial/(\partial z) & 0 & \partial/(\partial r) \\ \partial/(r\partial\theta) & (\partial/(\partial r) - 1/r) & 0 \\ 0 & \partial/(\partial z) & \partial/(r\partial\theta) \end{bmatrix} \begin{bmatrix} u \\ v \\ w \end{bmatrix} \quad (44)$$

The stress-strain relationship is given by Equation (26), $\sigma = \mathbf{D}(\epsilon - \epsilon_o) + \sigma_o$ where \mathbf{D} , the constitutive matrix, is expressed for isotropic material as [Timoshenko, 1970]:

$$\mathbf{D} = \frac{(1-\nu)E}{(1+\nu)(1-2\nu)} \begin{bmatrix} 1 & f & f & 0 & 0 & 0 \\ f & 1 & f & 0 & 0 & 0 \\ f & f & 1 & 0 & 0 & 0 \\ 0 & 0 & 0 & g & 0 & 0 \\ 0 & 0 & 0 & 0 & G & 0 \\ 0 & 0 & 0 & 0 & 0 & G \end{bmatrix} \quad (45)$$

where ν = poisson ratio, E = Young's modulus of elasticity for the material and G = shear modulus of elasticity. Also f and g can be expressed in terms of Poisson's ratio and Young's modulus as:

$$f = \frac{\nu}{1-\nu}, \quad g = \frac{(1-2\nu)}{2(1-\nu)} \quad (46)$$

The contribution of the n^{th} harmonic to the strain-displacement relationship is obtained by substituting Equation (41) through Equation (43) into Equation (44). This relationship can be expressed as $\epsilon_n = \mathbf{B}_n \mathbf{a}_n$, or more specifically for the symmetric component by:

$$\begin{bmatrix} \epsilon_r \\ \epsilon_\theta \\ \epsilon_z \\ \gamma_{rz} \\ \gamma_{r\theta} \\ \gamma_{\theta z} \end{bmatrix} = \begin{bmatrix} N_{1,z} \cos(n\theta) & 0 & 0 & \dots \\ \frac{N_1}{r} \cos(n\theta) & \frac{nN_1}{r} \cos(n\theta) & 0 & \dots \\ 0 & 0 & N_{1,z} \cos(n\theta) & \dots \\ N_{1,z} \cos(n\theta) & 0 & N_{1,z} \cos(n\theta) & \dots \\ \frac{-nN_1}{r} \sin(n\theta) & (N_{1,z} - \frac{N_1}{r}) \sin(n\theta) & 0 & \dots \\ 0 & N_{1,z} \sin(n\theta) & \frac{-nN_1}{r} \sin(n\theta) & \dots \end{bmatrix} \begin{bmatrix} u_1 \\ v_1 \\ w_1 \\ \dots \\ \dots \\ \dots \end{bmatrix}_{24 \times 1} \quad (47)$$

1, 2, 3, ..., 8

It should be noted that for antisymmetric harmonics, the \mathbf{B} matrix is obtained by interchanging the sine and cosine terms, and the last two rows are multiplied by negative sign. The stiffness matrix is obtained by substituting Equation (47) in Equation (34). One also finds that the stiffness matrix obtained for the symmetric and antisymmetric cases are identical. This is due to the nature of displacements given by Equations (41), (42) and (43). The stiffness matrix obtained above is only a function of n . Thus, the assembly of all individual stiffness matrices results in a system of uncoupled equations which can be solved independently for each n . The solutions obtained from the analyses are then superposed to get the overall result.

Appendix B Surface Traction and Load Distributions

This chapter discusses the theory required for the particular implementation of distributed surface tractions employed in this research. Strain and stress computations at any point on the surface are also discussed.

Discretization of Surface Traction

In general, the load vector \mathbf{f} given in Eq. (34) has contributions from body forces, surface tractions, residual stresses and strains, and concentrated forces. One can use any shape functions to interpolate the distributed loads, but in most cases the shape functions used are the same as those used to develop the stiffness matrix and the loads obtained are called consistent nodal loads. In this section, only the surface tractions for the eight noded element are discussed. Quadratic shape functions are used to interpolate the load distribution and hence the loads obtained are consistent [Bickford, 1990 and Cook, 1989].

Let $\mathbf{q}(s)$ represent the surface traction vector on side three of the element shown in Figure B-1. The vector $\mathbf{q}(s)$ has components $q_x(s)$ and $q_y(s)$. The variable s represents distance along the surface defined by nodes 3, 4, and 7. The contribution to the load vector from the loading on this element is then given as:

$$\mathbf{f}_s(s) = \int_s \mathbf{N}^T \mathbf{q}(s) ds \quad (48)$$

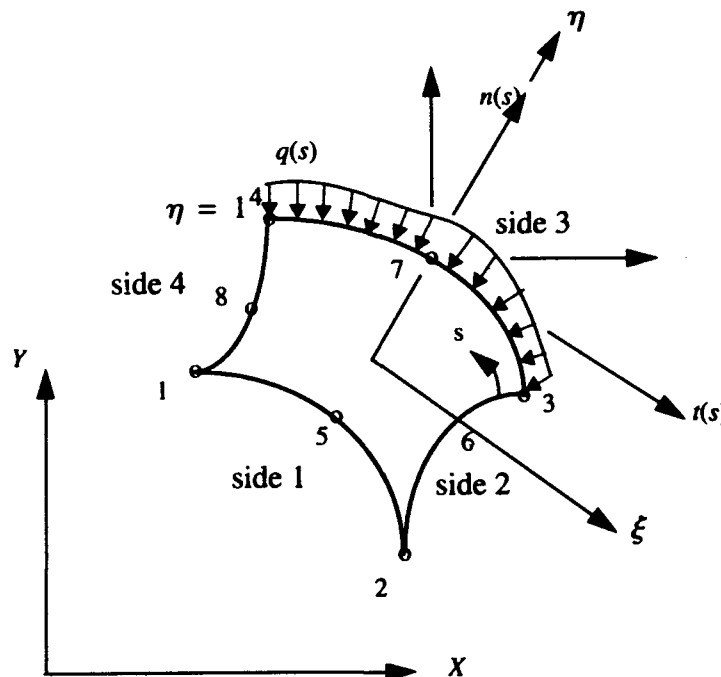


FIGURE B-1. Eight-Noded Isoparametric Element with a Load of $q(s)$.

where \mathbf{f}_s is a 6×1 vector of consistent nodal loads and \mathbf{N} is a 2×6 matrix of element shape functions. To employ gauss integration, a natural coordinate system, $\xi - \eta$, is introduced. In the natural coordinate system, the element is a 2×2 square where ξ and η each run from -1 to +1. Using the element shape functions to also define the mapping between physical coordinates and natural coordinates, x and y can be expressed as [Bickford, 1990]:

$$x = \sum_i N_i|_{\eta=1} x_i \quad (49)$$

and:

$$y = \sum_i N_i|_{\eta=1} y_i \quad (50)$$

The index i is summed over nodes 3, 4 and 7, the nodes on side 3. Note, also, that side 3 is defined in the natural coordinate system by $\eta = 1$. Further the derivatives of x and y with respect to ξ can be given by the following expressions:

$$\frac{dx}{d\xi} = \frac{\partial}{\partial \xi} \left[\sum_i N_i|_{\eta=1} x_i \right] \quad (51)$$

$$= A\xi + B \quad (52)$$

and:

$$\frac{dy}{d\xi} = \frac{\partial}{\partial \xi} \left[\sum_i N_i|_{\eta=1} y_i \right] \quad (53)$$

$$= C\xi + D \quad (54)$$

where $A = (x_3 - 2x_7 + x_4)$, $B = (x_3 - x_4)/2$, $C = (y_3 - 2y_7 + y_4)$ and $D = (y_3 - y_4)/2$. In the above, (x_i, y_i) are the coordinates of node i (either 3, 4 or 7). Similarly, the differential length ds can be given as:

$$ds = Jd\xi \quad (55)$$

where:

$$J = \left[\left(\frac{dx}{d\xi} \right)^2 + \left(\frac{dy}{d\xi} \right)^2 \right]^{1/2} \quad (56)$$

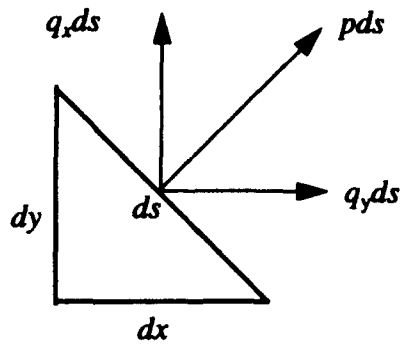


FIGURE B-2. Load $p ds$ Acting Over an Differential Element ds .

Furthermore the differential length ds can be integrated to get s , the distance along the surface from node 3, that is,

$$\begin{aligned}
 s &= \int_0^s ds \\
 &= \int_{-1}^{\xi} J d\xi
 \end{aligned}
 \tag{57}$$

Also, J can be expressed in terms of A , B , C and D as:

$$J = [(A^2 + C^2) \xi^2 + 2(AB + CD) \xi + (B^2 + D^2)]^{1/2}
 \tag{58}$$

It can be seen from Figure B-2 that:

$$q_x ds = p dy
 \tag{59}$$

and

$$q_y ds = p dx
 \tag{60}$$

Thus, the x and y components of the vector f can be written as:

$$f_{sx}^i = \int_s p(s) N_i dy
 \tag{61}$$

and:

$$f_{sy}^i = \int_s p(s) N_i dx \quad (62)$$

where again i is 3, 4, or 7. Using Equations (51) through (58), these integrals can be evaluated in the natural coordinate system as:

$$f_{sx}^i = \int_{-1}^1 p[s(\xi)] N_i(\xi) (C\xi + D) d\xi \quad (63)$$

and:

$$f_{sy}^i = \int_{-1}^1 p[s(\xi)] N_i(\xi) (A\xi + B) d\xi \quad (64)$$

Computation of Strains on the Surface of an Element

In general, strains are obtained from the discretized displacement field through use of the strain-displacement relation, $\epsilon = \mathbf{B}\mathbf{u}$, where ϵ = vector of strains, \mathbf{B} = strain-displacement matrix and \mathbf{u} = vector of nodal displacements [Cook, 1989; Timoshenko and Goodier, 1970]. The important question which arises here is which strains should be computed to get maximum accuracy. It can be shown that for isoparametric elements, strains are more accurate at the Gauss points of the quadrature rule one order less than that required for full integration of the element stiffness matrix (*i.e.*, the so-called Barlow points). However, in most cases the points of interest are not the Barlow points. In such cases, the strains are interpolated or extrapolated to any point of interest from the Barlow points [Barlow, 1976].

Extrapolation/Interpolation of Strain Tensor

Consider the eight noded isoparametric element depicted in Figure B-3. Generally, the order of the Gauss quadrature rule used to obtain the element stiffness matrix is 3 x 3. This means that the strains are more accurate at the 2 x 2 Gauss points. Furthermore, it can be deduced from the shape functions and the strain-displacement relationship that displacements are quadratic in nature and strains are linearly related. Hence, the strains at any point on the surface can be linearly interpolated from the Barlow points A, B, C, and D.

Consider the case where strains are to be derived at point P (see Figure B-2). This is done in two stages. At the first stage, strains are computed at the four Barlow points from the strain-displacement relationship. These points are represented in the $r-s$ coordinate system. The $r-s$ coordinate system is linearly related to the $\xi-\eta$ coordinate system by the following expression:

$$r = \sqrt{3}\xi \text{ and } s = \sqrt{3}\eta \quad (65)$$

In the second stage, the strains computed at the Barlow points are extrapolated to obtain the strains, ϵ_P , at point P via:

$$\epsilon_P = \sum_{i=1}^4 N_i \epsilon_i \quad (66)$$

where ϵ_i = vector of strain at the Barlow points and N_i = bilinear shape function given in the $r-s$ coordinate system for the four Barlow points A, B, C, and D. The shape functions are locally described as,

$$N_i = \frac{1}{4} (1 \pm r) (1 \pm s) \quad (67)$$

where r and s are the local coordinates of point P.

Computation of Strains at an Arbitrary Orientation on the Surface

Consider the situation where the direct strain has to be computed in the direction of unit vector g at an angle φ with respect to the unit base vector e_θ on the surface of an element (see Figure B-4). At any point on the surface a unit normal vector, n , and a unit tangential vector, e_t ,

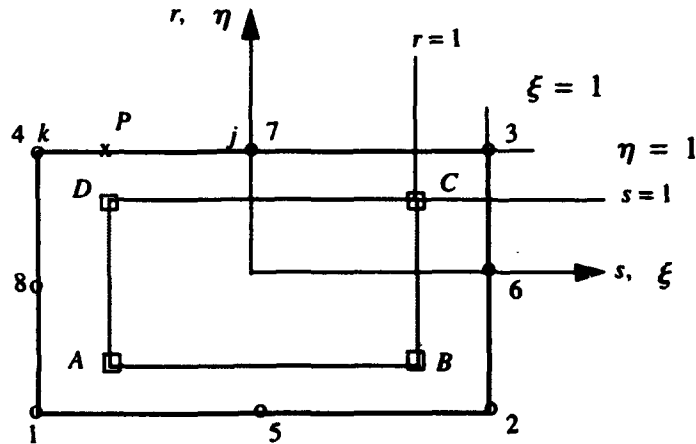


FIGURE B-3. Eight-Noded Element. A, B, C, and D are Barlow Points.

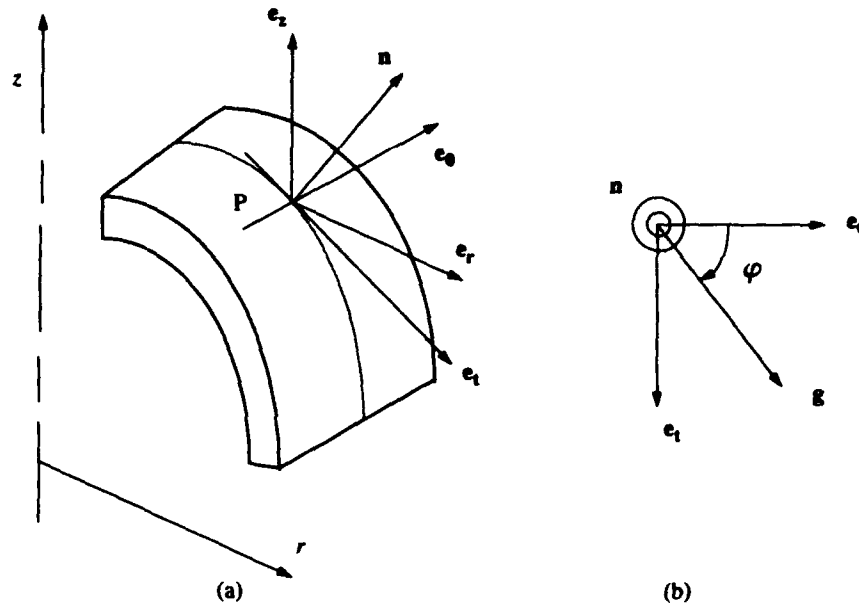


FIGURE B-4. (a) Axisymmetric Body (b) Direction of g at Which Strains are Computed.

are computed from the shape functions and the coordinates of nodes j, k and P (Figure B-5). It has to be noted that j and k are nodes of an element where P is any point on the surface. The coordinates of P are computed from Equations (49) and (50). Using Equations (51) through (56), the unit normal and tangential vectors are expressed as (see Figure B-4):

$$\mathbf{e}_n(\xi) = \frac{1}{\frac{ds}{d\xi}} \left\{ \frac{dx}{d\xi} \mathbf{e}_r + \frac{dy}{d\xi} \mathbf{e}_z \right\} \quad (68)$$

$$= l(\xi) \mathbf{e}_r + m(\xi) \mathbf{e}_z \quad (69)$$

and:

$$\mathbf{e}_t(\xi) = \frac{1}{\frac{ds}{d\xi}} \left\{ -\frac{dy}{d\xi} \mathbf{e}_r + \frac{dx}{d\xi} \mathbf{e}_z \right\} \quad (70)$$

$$= -m(\xi) \mathbf{e}_r + l(\xi) \mathbf{e}_z \quad (71)$$

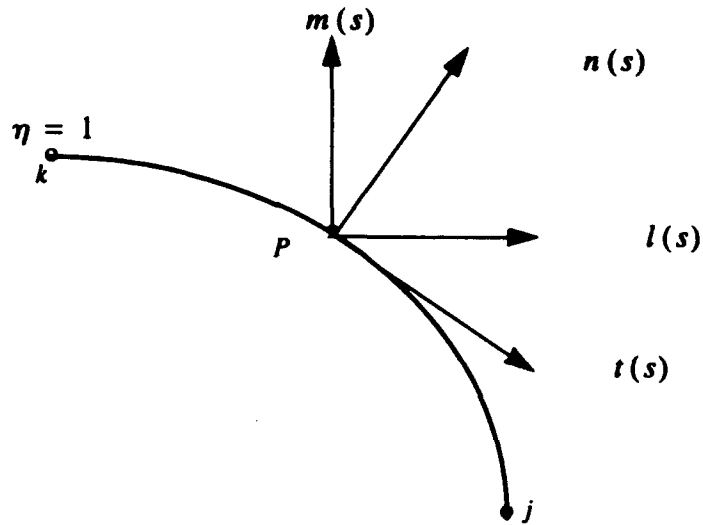


FIGURE B-5. Side of an Eight-Noded Isoparametric Element Where $\eta = 1$. Point P is Where Strains are Computed.

where e_r and e_z are unit vectors described in r and z direction, respectively. Furthermore $l(\xi)$ and $m(\xi)$ are described by :

$$l(\xi) = \frac{A\xi + B}{J} \quad (72)$$

and:

$$m(\xi) = \frac{C\xi + D}{J} \quad (73)$$

where A , B , C , and D have the same expression as defined in the beginning of Appendix B. From Figure B-4b it is noted that the vector g is at an angle φ with respect to e_θ in the $e_\theta - e_r$ plane. Thus:

$$g = \cos(\varphi) e_\theta + \sin(\varphi) e_r \quad (74)$$

Using Equation (71) and substituting in above equation, we have:

$$g = -m(\xi) \sin(\varphi) e_r + \cos(\varphi) e_\theta + l(\xi) \sin(\varphi) e_z \quad (75)$$

or in matrix notation:

$$\mathbf{g} = [-m(\xi) \sin(\varphi) \cos(\varphi) l(\xi) \sin(\varphi)]^T \quad (76)$$

where again \mathbf{e}_θ is a unit vector in the θ direction. Furthermore, it can be shown that the required strain vector λ can be expressed as:

$$\lambda = \mathbf{g}^T \bar{\boldsymbol{\epsilon}} \mathbf{g} \quad (77)$$

where $\bar{\boldsymbol{\epsilon}}$ is the strain tensor described in the cylindrical coordinate system by the following matrix,

$$\bar{\boldsymbol{\epsilon}} = \begin{bmatrix} \epsilon_r & \frac{\gamma_{r\theta}}{2} & \frac{\gamma_{rz}}{2} \\ \frac{\gamma_{r\theta}}{2} & \epsilon_\theta & \frac{\gamma_{z\theta}}{2} \\ \frac{\gamma_{rz}}{2} & \frac{\gamma_{\theta z}}{2} & \epsilon_z \end{bmatrix} \quad (78)$$